Original Article

MOLECULAR METABOLISM

The type 2 diabetes gene product STARD10 is a phosphoinositide-binding protein that controls insulin secretory granule biogenesis

Gaelle R. Carrat [1], Elizabeth Haythorne [1], Alejandra Tomas [1], Leena Haataja [2], Andreas Müller [3,4,5,6], Peter Arvan [2], Alexandra Piunti [1,7], Kaiying Cheng [8], Mutian Huang [1], Timothy J. Pullen [1,9], Eleni Georgiadou [1], Theodoros Stylianides [10], Nur Shabrina Amirruddin [11,12], Victoria Salem [1,13], Walter Distaso [14], Andrew Cakebread [15], Kate J. Heesom [16], Philip A. Lewis [16], David J. Hodson [17,18,19], Linford J. Briant [20], Annie C.H. Fung [21], Richard B. Sessions [22], Fabien Alpy [23], Alice P.S. Kong [21], Peter I. Benke [24], Federico Torta [24], Adrian Kee Keong Teo [11,12,25], Isabelle Leclerc [1], Michele Solimena [3,4,5,6], Dale B. Wigley [8], Guy A. Rutter [1,*]

ABSTRACT

Objective: Risk alleles for type 2 diabetes at the *STARD10* locus are associated with lowered *STARD10* expression in the β-cell, impaired glucose-induced insulin secretion, and decreased circulating proinsulin:insulin ratios. Although likely to serve as a mediator of intracellular lipid transfer, the identity of the transported lipids and thus the pathways through which STARD10 regulates β-cell function are not understood. The aim of this study was to identify the lipids transported and affected by STARD10 in the β-cell and the role of the protein in controlling proinsulin processing and insulin granule biogenesis and maturation.

Methods: We used isolated islets from mice deleted selectively in the β-cell for *Stard10* (β*Stard10*KO) and performed electron microscopy, pulse-chase, RNA sequencing, and lipidomic analyses. Proteomic analysis of STARD10 binding partners was executed in the INS1 (832/13) cell line. X-ray crystallography followed by molecular docking and lipid overlay assay was performed on purified STARD10 protein.

Results: β*Stard10*KO islets had a sharply altered dense core granule appearance, with a dramatic increase in the number of "rod-like" dense cores. Correspondingly, basal secretion of proinsulin was increased versus wild-type islets. The solution of the crystal structure of STARD10 to 2.3 Å resolution revealed a binding pocket capable of accommodating polyphosphoinositides, and STARD10 was shown to bind to inositides phosphorylated at the 3' position. Lipidomic analysis of β*Stard10*KO islets demonstrated changes in phosphatidylinositol levels, and the inositol lipid kinase PIP4K2C was identified as a STARD10 binding partner. Also consistent with roles for STARD10 in phosphoinositide signalling, the phosphoinositide-binding proteins *Pirt* and *Synaptotagmin 1* were amongst the differentially expressed genes in β*Stard10*KO islets.

Conclusion: Our data indicate that STARD10 binds to, and may transport, phosphatidylinositides, influencing membrane lipid composition, insulin granule biosynthesis, and insulin processing.

Keywords Type 2 diabetes; Pancreatic β-cell; Lipid transporter; Insulin granule biogenesis; Phosphoinositides

[1]Section of Cell Biology and Functional Genomics, Imperial College London, du Cane Road, London, W12 0NN, UK [2]Division of Metabolism, Endocrinology & Diabetes, Department of Internal Medicine, University of Michigan Medical School, Ann Arbor, MI, USA [3]Molecular Diabetology, University Hospital and Faculty of Medicine Carl Gustav Carus, TU Dresden, Dresden, Germany [4]Paul Langerhans Institute Dresden (PLID) of the Helmholtz Center Munich, University Hospital Carl Gustav Carus and Faculty of Medicine of the TU Dresden, Dresden, Germany [5]German Center for Diabetes Research (DZD e.V.), Neuherberg, Germany [6]Max Planck Institute of Molecular Cell Biology and Genetics (MPI-CBG), Dresden, Germany [7]Lille 1 University-Science and Technology, Cité Scientifique, 59655, Villeneuve d'Ascq Cedex, France [8]Section of Structural Biology, Department of Medicine, Imperial College London, London, UK [9]Department of Diabetes, Faculty of Life Science and Medicine, King's College London, London, UK [10]Loughborough University, Centre of Innovative and Collaborative Construction Engineering, Leicestershire, LE11 3TU, UK [11]Stem Cells and Diabetes Laboratory, Institute of Molecular and Cell Biology (IMCB), A*STAR, Proteos, Singapore, 138673, Singapore [12]Department of Medicine, Yong Loo Lin School of Medicine, National University of Singapore, Singapore, 119228, Singapore [13]Section of Investigative Medicine, Department of Medicine, Imperial College London, du Cane Road, London, W12 0NN, UK [14]Imperial College Business School, Imperial College London, Exhibition Road, London, SW7 2AZ, UK [15]London Metallomics Facility, King's College London, Strand, London, WC2R 2LS, UK [16]Proteomics Facility, University of Bristol, Bristol, UK [17]Centre for Endocrinology, Diabetes and Metabolism, Birmingham Health Partners, Birmingham, UK [18]Institute of Metabolism and Systems Research, University of Birmingham, Edgbaston, UK [19]Centre of Membrane Proteins and Receptors, University of Birmingham and University of Nottingham, Midlands, UK [20]Oxford Centre for Diabetes, Endocrinology, and Metabolism, Radcliffe Department of Medicine, University of Oxford, Churchill Hospital, Oxford, OX3 7LE, UK [21]Department of Medicine and Therapeutics, The Chinese University of Hong Kong, Shatin, Hong Kong [22]School of Biochemistry, Faculty of Life Sciences, University of Bristol, Bristol, BS8 1TD, UK [23]Institut de Génétique et de Biologie Moléculaire et Cellulaire (IGBMC), Institut National de la Santé et de la Recherche Médicale (INSERM) U1258, Centre National de la Recherche Scientifique (CNRS), UMR 7104, Université de Strasbourg, 1 rue Laurent Fries, 67404 Illkirch, France [24]Singapore Lipidomics Incubator, Department of Biochemistry, Yong Loo Lin School of Medicine, National University of Singapore, 8 Mdical Drive, Singapore, 117596, Singapore [25]Department of Biochemistry, Yong Loo Lin School of Medicine, National University of Singapore, Singapore, 117596, Singapore

*Corresponding author. +44 (0)20 7594 3340. E-mail: g.rutter@imperial.ac.uk (G.A. Rutter).

Received February 28, 2020 • Revision received April 24, 2020 • Accepted May 5, 2020 • Available online 13 May 2020

https://doi.org/10.1016/j.molmet.2020.101015

Abbreviations

BUDE	Bristol University Docking Engine
GFP	Green Fluorescent Protein
GWAS	Genome-Wide Association Study
K_{ATP}	ATP-sensitive K^+ channels
HRP	Horseradish Peroxidase
Kir6.2, *Kcnj11*	Potassium Inwardly Rectifying Channel Subfamily J Member 11
KOMP	NIH Knockout Mouse Project
ICP/MS	inductively coupled plasma mass spectrometry
IMPC	International Mouse Phenotyping Consortium
LPC	lysophosphatidylcholine
MBP	Maltose Binding Protein
PC	phosphatidylcholine
PE	phosphatidylethanolamine
PI	phosphatidylinositol
PI(3)P	phosphatidylinositol 3-phosphate
PI(4,5)P2	PIP_2, phosphatidylinositol 4,5-bisphosphate
PI(5)P	phosphatidylinositol 5-phosphate
PIP	phosphatidylinositol phosphate, phosphatidylinositide
Pip4k2c	phosphatidylinositol 5-phosphate 4-kinase type-2 gamma
Pirt	phosphoinositide-interacting regulator of transient receptor potential channels
RNAseq	RNA sequencing
Ptbp1	polypyrimidine tract-binding protein 1
Slc30a8	ZnT8, Solute Carrier Family 30 Member 8
SNARE	Soluble N-ethylmaleimide sensitive factor Attachment protein Receptor
STARD10	StAR Related Lipid Transfer Domain Containing 10
Syt1	synaptotagmin 1
Sytl4	synaptotagmin-like 4, granuphilin
TMT	Tandem Mass Tag
TRP	transient receptor potential

1. INTRODUCTION

Diabetes mellitus is characterised by high blood glucose and currently affects around 8.5% of the population worldwide. Normal glucose homeostasis requires the processing of proinsulin and the storage of the mature hormone within dense core granules in the pancreatic β-cell [1]. Glucose-induced insulin secretion involves glucose uptake and metabolism through the glycolytic pathway, increased ATP production by the mitochondria, and the closure of ATP-sensitive K^+ channels (K_{ATP}). Subsequent depolarisation of the plasma membrane leads to the opening of voltage-gated Ca^{2+} channels, Ca^{2+}-dependent assembly of the SNARE (SNAP (Soluble NSF Attachment Protein) Receptor) complex, and exocytosis [2]. In the intact islet, β-cell−β-cell connections allow coordinated insulin secretion through the propagation of Ca^{2+} and other signals [3–5], a process impaired by glucolipotoxicity [6] and affected by genes implicated in diabetes risk through genome-wide association studies (GWAS) such as *ADCY5* [7] and *TCF7L2* [8].

We have recently examined a T2D-associated locus adjacent to *STARD10* on chromosome 11q13 [9,10]. Risk variants at this locus were associated with a decrease in *STARD1*0 mRNA in human islets, with no concomitant change in the liver. Changes in the expression of the nearby *ARAP1* gene were not associated with the possession of risk alleles in either tissue, pointing to STARD10 as the mediator of the effects of risk variants. Providing further compelling evidence for *STARD10* as an "effector" gene, mice deleted for *Stard10* specifically in the β-cell recapitulated the features observed in the human carriers of the risk allele, with an increase in fed glycemia and a decrease in the plasma proinsulin:insulin ratio. Islets isolated from the knockout mice also showed impaired glucose-induced Ca^{2+} signalling and insulin secretion. Thus, β-cell STARD10 may be a useful therapeutic target in some forms of type 2 diabetes, particularly in risk allele carriers who may benefit from a tailored, pharmacogenetic approach.

STARD10 (previously named phosphatidylcholine transfer protein-like, Pctp-l) is a phospholipid transfer protein possessing a steroidogenic acute regulatory protein- (StAR-) related lipid transfer (START) domain that facilitates the transport of phosphatidylcholine and phosphatidylethanolamine between intracellular membranes [11]. Nevertheless, the molecular mechanisms by which STARD10 regulates insulin secretion in the β-cell, as well as its subcellular localisation and target membranes, remain unknown. We, therefore, examined in detail here the role of STARD10 in controlling the lipid composition, granule maturation, proinsulin processing, and metal ion homeostasis in the mouse β-cell. We reveal an unexpected role for STARD10 in binding inositol phospholipids which may contribute to both secretory granule biogenesis and intracellular signalling.

2. MATERIAL AND METHODS

2.1. Generation and use of Stard10 null mice

All animal procedures were approved by the UK Home Office according to the Animals (Scientific Procedures) Act 1986 of the United Kingdom (PPL PA03F7F0F to I. L.). *Stard10* whole body and conditional KO mice (C57BL/6NTac background) were generated by the trans-NIH Knockout Mouse Project (KOMP) and obtained from the KOMP Repository via the International Mouse Phenotyping Consortium (IMPC). Mice homozygous for floxed *Stard10* (Stard10$^{tm1c(KOMP)Wtsi}$, i.e., *Stard10*$^{fl/fl}$) alleles were crossed to mice expressing *Cre* recombinase from the endogenous *Ins1* locus (*Ins1-Cre* mice). This generated *Stard10*$^{fl/fl}$:*Ins1Cre*$^{+}$ (β*Stard10*KO) mice as in [9].

2.2. Islet isolation and culture

Mice were euthanized by cervical dislocation and pancreatic islets isolated by collagenase digestion as previously described [12] and cultured in RPMI 1640 medium, 11 mM glucose, supplemented with 10% (v/v) fetal bovine serum plus penicillin (100 units/mL), and streptomycin (0.1 mg/mL) at 37 °C in an atmosphere of humidified air (95%) and CO_2 (5%).

2.3. Transmission electron microscopy (EM) imaging

For conventional EM, islets were chemically fixed in 2% paraformaldehyde (EM grade), 2% glutaraldehyde, and 3 mM $CaCl_2$ in 0.1 M cacodylate buffer for 2 h at room temperature, then left overnight at 4 °C in a fresh fixative solution, osmicated, enrobed in agarose plugs, dehydrated in ethanol, and embedded in Epon. Epon was polymerised overnight at 60 °C. Ultrathin 70 nm sections were cut with a diamond knife (DiATOME) in a Leica Ultracut UCT ultramicrotome before the examination on an FEI Tecnai G2 Spirit TEM. Images were acquired in a charge-coupled device camera (Eagle) and processed using ImageJ.

2.4. Measurements of islet Zn^{2+} concentrations

2.4.1. Cytosolic free Zn^{2+} measurements

Imaging of cytosolic [Zn^{2+}] using the eCALWY4 sensor was carried out on mouse islets dispersed onto coverslips as previously described [13]. Cells were maintained at 37 °C and Krebs-HEPES-bicarbonate buffer (11 mM) was perifused with additions as stated in the figure. Images were captured at 433 nm monochromatic excitation wavelength. The acquisition rate was 20 images/min.

Image analysis was performed with ImageJ software [14] using a homemade macro, and the fluorescence emission ratios were derived after subtracting the background. We observed that during acquisition, photobleaching gradually decreased the steady-state ratio with a linear kinetic (not shown). This drift was thus, when necessary, corrected in the function of time with a constant factor.

2.4.2. Measurement of islet zinc content by inductively coupled plasma mass spectrometry (ICP-MS)

Mouse islets were washed twice in PBS and stored at −80 °C until ready to process. Islets were lysed in 100 μL nitric acid (trace metal grade) and heated at 50 °C for 6 h. The samples were then cooled and diluted in trace metal grade water up to a final volume of 1.3 mL, and 10 μL of 1000 ppb mix of 5 internal standards (bismuth, indium, scandium, terbium, and yttrium) was added. Standards between 0.5 and 500.5 μg/L of Zn were used for calibration. Samples were run on the Perkin Elmer NexION 350D using the Syngistix software.

2.5. Metabolic labelling of mouse pancreatic islets

Islets isolated from β*Stard10*KO and WT littermate mice were recovered overnight in RPMI-1640 medium containing 11 mM glucose plus 10% FBS and penicillin-streptomycin. In each case, 50 islets were washed twice in prewarmed RPMI lacking cysteine and methionine. Islets were pulse-labelled with ^{35}S-labelled amino acids for 20 min and chased for 1.5 h or 4 h in 5 mM glucose RPMI-1640 plus 10% FBS, Hepes, Pyruvate, and penicillin-streptomycin. Islets were lysed in radioimmunoprecipitation assay buffer (25 mmol/L Tris, pH 7.5; 1% Triton X-100; 0.2% deoxycholic acid; 0.1% SDS; 10 mmol/L EDTA; and 100 mmol/L NaCl) plus 2 mmol/L N-ethylmaleimide and protease inhibitor cocktail. Both cell lysates and media were precleared with Pansorbin and immunoprecipitated with anti-insulin antibodies and protein A agarose overnight at 4 °C. Immunoprecipitates were analysed using tris-tricine-urea-SDS-PAGE under nonreducing conditions or SDS-PAGE on 4–12% acrylamide gradient gels (NuPAGE) under reducing conditions as indicated with phosphorimaging. Bands were quantified using ImageJ software.

2.6. *In vitro* proinsulin and insulin measurements

Islets (10/well) were incubated in triplicate for each condition and treatment. Islets were preincubated for 1 h in 3 mM glucose Krebs-Ringer-Hepes-Bicarbonate (KRH) buffer prior to secretion assay (30 min) in 3 mM or 17 mM glucose. The secretion medium was then collected to measure the insulin and proinsulin concentrations using an insulin HTRF kit (Cisbio Bioassays) and a rat/mouse proinsulin ELISA kit (Mercodia), respectively.

2.7. Lipidomic analysis

Islets isolated from β*Stard10*KO and WT littermate mice were recovered overnight in RPMI-1640 medium containing 11 mM glucose plus 10% FBS and penicillin-streptomycin. Islets were then washed twice in PBS, snap-frozen in a bath of ethanol and dry ice, and kept at −80 °C until ready to process. Lipids were extracted with 100 μL 1-butanol/methanol (1:1, v/v) containing 2.5 μL of SPLASH™ Lipidomix® Mass Spec Standard I and 2.5 μL Cer/Sph Mixture I, purchased from Avanti Polar Lipids. The mixture was vortexed for 30 s, sonicated for 30 min at 20 °C, and then centrifuged at 14 000 g for 10 min. The supernatant was transferred into vials. The lipidomic analysis was performed by the Singapore Lipidomics Incubator (SLING) using an Agilent 1290 Infinity II LC system combined with an Agilent 6495 triple quadrupole mass spectrometer. Reversed-phase chromatographic separation of 1 μL samples was carried out on an Agilent Zorbax RRHD Eclipse Plus C18, 95 Å (50 × 2.1 mm, 1.8 μm) column maintained at 40 °C. The mobile phases consisted of (A) 10 mmol/L ammonium formate in acetonitrile/water (40:60, v/v) and (B) 10 mmol/L ammonium formate in acetonitrile/2-propanol (10:90, v/v). Using a flow rate of 0.4 mL/min, the gradient elution program included 20% B to 60% B from 0 to 5 min and 60%B to 100% B from 2 to 7 min, where it was maintained till 9 min, and then reequilibrated at 20% B for 1.8 min prior to the next injection. All samples were kept at 10 °C in the autosampler. The lipid amounts were normalised to protein content. MRM chromatograms obtained in positive ion mode, covering >10 lipid classes, were processed using Agilent MassHunter Quantitative Analysis software (version B.08.00). Peaks were annotated based on retention time and specific MRM transitions.

2.8. Massive parallel sequencing of RNA (RNAseq)

Total RNA was extracted with TRIzol from isolated mouse islets. Polyadenylated transcripts were selected during the preparation of paired-end, directional RNAseq libraries using the Illumina TruSeq Stranded mRNA Library Prep Kit. Libraries were sequenced on an Illumina HiSeq 4000 machine at 75 bp paired-end read length. The quality of the sequenced libraries was assessed using fastQC. Reads were mapped to the Grc38m assembly using HiSat2. Annotated transcripts were quantified using featureCounts, and differentially expressed genes were identified with DESeq2. Raw sequence data for RNAseq will be made available via the deposition to ArrayExpress.

2.9. Purification and identification of STARD10 interacting proteins by mass spectrometry

2.9.1. Co-immunoprecipitation

INS1 (832/13) cells were lysed in the following nondenaturing lysis buffer: 20 mM HEPES, 150 mM NaCl, 1% Igepal, protease inhibitors (Roche Diagnostics, complete, EDTA-free protease inhibitor cocktail tablets), and phosphatase inhibitors (Sigma, P5726). 6 μg of Rabbit IgG Isotype Control (Abcam, ab171870) or anti-PCTP-L (STARD10) antibody (Abcam. ab242109) was bound to 50 μL of Dynabeads Protein A for 1 h at 4 °C. For co-immunoprecipitation (Co-IP), 1 mg of protein lysate was incubated with the complex beads-antibodies overnight at 4 °C. Beads were then washed twice in lysis buffer and twice in PBS-Tween 0.01% prior to proteomic analysis by the Bristol Proteomics Facility.

2.9.2. TMT labelling and high pH reversed-phase chromatography

Pull-down samples were reduced (10 mM TCEP 55 °C, 1 h), alkylated (18.75 mM iodoacetamide, room temperature, 30 min), digested on the beads with trypsin (2.5 μg trypsin; 37 °C, overnight), and then labelled with Tandem Mass Tag (TMT) six-plex reagents according to the manufacturer's protocol (Thermo Fisher Scientific, Loughborough LE11 5RG, UK), and the labelled samples were pooled.

The pooled sample was evaporated to dryness, resuspended in 5% formic acid, and then desalted using a SepPak cartridge according to the manufacturer's instructions (Waters, Milford, Massachusetts, USA).

The eluate from the SepPak cartridge was again evaporated to dryness and resuspended in buffer A (20 mM ammonium hydroxide, pH 10) prior to fractionation by high pH reversed-phase chromatography using an UltiMate 3000 liquid chromatography system (Thermo Fisher Scientific). In brief, the sample was loaded onto an XBridge BEH C18 Column (130 Å, 3.5 μm, 2.1 mm × 150 mm, Waters, UK) in buffer A and peptides eluted with an increasing gradient of buffer B (20 mM Ammonium Hydroxide in acetonitrile, pH 10) from 0% to 95% over 60 min. The resulting fractions (4 in total) were evaporated to dryness and resuspended in 1% formic acid prior to analysis by nano-LC MSMS using an Orbitrap Fusion Tribrid Mass Spectrometer (Thermo Scientific).

2.9.3. Nano-LC mass spectrometry

High pH RP fractions were further fractionated using an Ultimate 3000 nano-LC system in line with an Orbitrap Fusion Tribrid Mass Spectrometer (Thermo Scientific). In brief, peptides in 1% (vol/vol) formic acid were injected onto an Acclaim PepMap C18 nano-trap column (Thermo Scientific). After washing with 0.5% (vol/vol) acetonitrile, 0.1% (vol/vol) formic acid peptides were resolved on a 250 mm × 75 μm Acclaim PepMap C18 reversed-phase analytical column (Thermo Scientific) over a 150 min organic gradient, using 7 gradient segments (1%–6% solvent B over 1 min, 6%–15% B over 58 min, 15%–32% B over 58 min, 32%–40% B over 5 min, 40%–90% B over 1 min, held at 90% B for 6 min, and then reduced to 1% B over 1 min) with a flow rate of 300 nL min^{-1}. Solvent A was 0.1% formic acid and solvent B was aqueous 80% acetonitrile in 0.1% formic acid. Peptides were ionized by nanoelectrospray ionization at 2.0 kV using a stainless steel emitter with an internal diameter of 30 μm (Thermo Scientific) and a capillary temperature of 275 °C.

All spectra were acquired using an Orbitrap Fusion Tribrid Mass Spectrometer controlled by Xcalibur 3.0 software (Thermo Scientific) and operated in data-dependent acquisition mode using an SPS-MS3 workflow. FTMS1 spectra were collected at a resolution of 120 000, with an automatic gain control (AGC) target of 400 000 and max injection time of 100 ms. Precursors were filtered with an intensity range from 5000 to 1E20, according to charge state (to include charge states 2–6) and with monoisotopic peak determination set to the peptide. Previously interrogated precursors were excluded using a dynamic window (60 s ± 10 ppm). The MS2 precursors were isolated with a quadrupole isolation window of 1.2m/z. ITMS2 spectra were collected with an AGC target of 10 000, max injection time of 70 ms, and CID collision energy of 35%.

For FTMS3 analysis, the Orbitrap was operated at a resolution of 30 000 with an AGC target of 50 000 and a max injection time of 105 ms. Precursors were fragmented by high-energy collision dissociation (HCD) at a normalised collision energy of 55% to ensure maximal TMT reporter ion yield. Synchronous Precursor Selection (SPS) was enabled to include up to 5 MS2 fragment ions in the FTMS3 scan.

2.9.4. Data analysis

The raw data files were processed and quantified using Proteome Discoverer software v2.1 (Thermo Scientific) and searched against the UniProt Rat database (downloaded in January 2019; 35759 entries) using the SEQUEST algorithm. Peptide precursor mass tolerance was set at 10 ppm, and MS/MS tolerance was set at 0.6 Da. Search criteria included oxidation of methionine (+15.9949) as a variable modification and carbamidomethylation of cysteine (+57.0214) and the addition of the TMT mass tag (+229.163) to peptide N-termini and lysine as fixed modifications. Searches were performed with full tryptic digestion and a maximum of 2 missed cleavages were allowed. The reverse database search option was enabled and all data were filtered to satisfy false discovery rate (FDR) of 5%.

2.10. Lipid overlay assay

All incubation steps were performed at room temperature. PIP strips (Thermo Scientific) were blocked for 1 h in TBS containing 0.1% Tween-20 (TBS-T) supplemented by 3% fatty-acid-free BSA (Sigma Aldrich) before incubation with the purified STARD10 protein (1 μg/mL in TBS-T + 3% BSA) for 1 h. The membrane was washed 5 times for 10 min in TBS-T and probed for 1 h with the polyclonal goat anti-STARD10 antibody (Santa Cruz sc54336; 1/1000 in TBS-T + 3% BSA). After 5 washes for 10 min in TBS-T, the membrane was incubated for 1 h with the horseradish peroxidase-conjugated donkey anti-goat IgG (Santa Cruz sc2020; 1/2000 in TBS-T + 3%BSA). After 5 washes for 10 min in TBS-T, bound proteins were detected by ECL reagent (GE Healthcare).

2.11. Structure solution of STARD10

2.11.1. Cloning

The full-length gene encoding human STARD10 protein was amplified from cDNA by PCR and cloned into a modified pET28a expression vector, pET28-HMT, which contains a fused N-terminal 6 × His-tag, an MBP-tag, and a TEV protease recognition site (His-MBP-TEV) by In-fusion® HD Cloning kit (Takara Bio, USA). The fidelity of the constructs was confirmed by gel electrophoresis and sequencing.

2.11.2. Protein preparation

In brief, transformed *E. coli* BL21 (DE3) clones were grown at 37 °C in LB medium containing 50 μg/mL Kanamycin to an optical density at 600 nm of 0.8. Protein expression was induced at 30 °C for 4 h by adding isopropyl-β-D-thiogalactopyranoside (IPTG) to a final concentration of 0.5 mM. After harvesting, cells were resuspended in lysis buffer (20 mM Tris (pH 8.0), 1 M NaCl, and 0.5 mM TCEP) with protease inhibitor, lysed by sonication, and centrifuged at 18 000×*g* for 60 min at 4 °C. The supernatant was loaded on a HisTrap HP column (GE Healthcare, Fairfield, CT), equilibrated with buffer A (20 mM Tris (pH 8.0), 1 M NaCl, 0.5 mM TCEP, and 5 mM imidazole), washed with 30 mM imidazole, and finally eluted with 500 mM imidazole. After His-MBP-TEV-tag removal using TEV protease, the protein was dialysed into buffer B (20 mM Tris (pH 8.0), 100 mM NaCl, and 0.5 mM TCEP) and reloaded onto the HisTrap HP column (GE Healthcare) to remove the tag, uncleaved protein, and TEV protease. The flow-through fractions were collected and loaded onto a MonoQ column (GE Healthcare) preequilibrated with buffer B. Some *E. coli* background protein and DNA rather than STARD10 can bind on the MonoQ. Then, the flow-through fractions were collected and loaded onto a Heparin HP column (GE Healthcare) preequilibrated with buffer B. Fraction containing STARD10 protein was eluted with a linear gradient from 250 mM to 800 mM NaCl. The protein was finally purified by Superdex 75 10/300 GL column (GE Healthcare) with buffer B.

2.11.3. Crystallisation and structure determination

Crystallisation trials were carried out by sitting drop vapour diffusion method at 293 K. Freshly purified STARD10 was concentrated to ~38 mg/mL and centrifuged to remove insoluble material before crystallisation. Single crystals appeared in condition containing 50% (v/v) PEG 200, 100 mM sodium phosphate dibasic/potassium phosphate monobasic (pH 6.2), and 200 mM NaCl after one month. Cryo-freezing was achieved by stepwise soaking the crystals in reservoir solution

containing 10, 20, and 30% (w/v) glycerol for 3 min and flash freezing in liquid nitrogen. X-ray diffraction data were collected on beamline I03 at the Diamond synchrotron X-ray source and were integrated and scaled with the Xia2 system [15].
The structure was determined by molecular replacement using the START domain structure from human STARD5 protein (PDB ID: 2R55) as a search model in CCP4, followed by rigid-body refinement by Refmac5 [16]. The structure was refined using PHENIX [17] and interspersed with manual model building using COOT [18]. The structure contains one STARD10 molecule in the asymmetric unit. 245 out of 291 residues (STARD10 full length) were successfully built into the density in the final structure. The statistics for data collection and model refinement are listed in Supplemental Table 2.

2.12. Molecular docking of ligands in STARD10 and STARD2

In silico molecular docking was performed using the Bristol University Docking Engine (BUDE 1.2.9). Firstly, a set of conformations for the head groups, glycero-inositol-1-phosphate and glycero-3-phosphoinositol-1-phosphate, were generated using OpenBabel (2.4.1) giving 87 and 85 conformers, respectively. The docking grid was centred on the central cavity in STARD2 (1LNL) and STARD10 (6SER). Each conformer of the PI and PI(3)P head groups was docked into both structures. Each docking run found the best solutions by sampling a total of 1.1 million poses via BUDE's genetic algorithm. Final models were constructed by adding the 2 linoleoyl chains from the conformation in 1LN1 (STARD2 dilinoleoylphosphatidylcholine complex) and refined by energy minimisation with GROMACS.

2.13. Statistics

Data are expressed as mean ± SD. The normality of the data distribution was tested by D'Agostino and Pearson and Shapiro—Wilk normality tests. For normally distributed data, significance was tested by Student's two-tailed *t*-test or Welch's *t*-test if the variances were found significantly different by *F*-test. Mann—Whitney test was used for nonparametric data, and one- or two-way ANOVA with SIDAK multiple comparison test was used for comparison of more than two groups, using Graphpad Prism 7 software. $P < 0.05$ was considered significant.

3. RESULTS

3.1. *Stard10* deletion affects dense core granule ultrastructure

As an initial approach to determining the target membranes for STARD10 action, we first explored the impact of deleting the *Stard10* gene on β-cell ultrastructure. We have previously shown that crossing of *Stard10* floxed mice to Ins1Cre knock-in mice [19] efficiently and selectively deletes STARD10 in the pancreatic β-cell [9]. Transmission EM images of β-cells in islets isolated from β*Stard10*KO mice revealed a dramatic change in insulin granule morphology with a significant increase in "atypical" granules with a "rod-shaped" core (Figure 1A,B; β*Stard10*KO: 12.05 ± 1.67% versus *Ctl*: 2.78 ± 0.36%; $P < 0.001$, Student's *t*-test, $n = 3$ animals). In addition, the mean granule diameter was decreased (Figure 1C; β*Stard10*KO: 255.2 ± 25.8 nm versus *Ctl*: 277.9 ± 24.9 nm; $P < 0.001$, Student's *t*-test, $n = 42$ images from 3 animals) and the "circularity" increased slightly (Figure 1D; β*Stard10*KO: 0.89 ± 0.01 versus *Ctl*: 0.87 ± 0.03; $P < 0.05$, Welch's *t*-test, $n = 42$ images from 3 animals) in β*Stard10*KO compared to WT littermate β-cells. However, the cytoplasmic abundance of granule profiles ("density") (Figure 1E; *Ctl*: 3.82 ± 1.80 versus β*Stard10*KO: 3.66 ± 0.61 granules/μm^2; ns, Mann—Whitney test, $n = 19$ images from 3 animals) and the number of granules morphologically docked to the plasma membrane (Figure 1F; *Ctl*: 0.76 ± 0.43 versus β*Stard10*KO: 0.75 ± 0.28 granules/μm plasma membrane; ns, Mann—Whitney test, $n = 18$ images from 3 animals; granules were considered morphologically docked if the distance from their centre to the plasma membrane was ≤200 nm) remained similar in both genotypes.
The analyses of transmission EM images of human β-cells from partially pancreatectomised patient samples (Supplemental Figure 1A and Supplemental Table 1) showed no significant correlation between *STARD10* expression measured by RNAseq and the percentage of mature granules (Supplemental Figure 1B) or the density of mature, immature, or total granules (Supplemental Figure 1C).
Thus, deleting *Stard10* specifically in the β-cell in mice greatly affected the insulin granule ultrastructure and overall shape with an increase in granules with a "rod-shaped" core.

3.2. Islet zinc content is increased in β*Stard10*KO mice

To determine whether the abnormalities in granule structure may result from altered Zn^{2+} content of granules, itself a critical regulator of insulin crystallisation [1,20], we used the Förster resonance energy transfer- (FRET-) based sensor eCALWY4 [13] to measure free Zn^{2+} concentration in the cytosol of dissociated islets from β*Stard10*KO mice. The measured free cytosolic Zn^{2+} concentrations were similar in both genotypes (Figure 1G,H; ns; Mann—Whitney test, $n = 33$—65 cells). On the other hand, total zinc, measured by inductively coupled plasma mass spectrometry (ICP/MS), was higher in β*Stard10*KO isolated islets compared to WT ones (Figure 1I: *Ctl*: 90.1 ± 55.15 versus β*Stard10*KO: 183.4 ± 38.73 μg/mL; $P < 0.05$; unpaired *t*-test, $n = 4$ animals).

3.3. Newly synthesised proinsulin is constitutively secreted by β*Stard10*KO islets

The characteristic decrease of plasma proinsulin:insulin ratio observed in human carriers of the risk alleles at this locus [21] and the observation of a similar phenotype in β*Stard10*KO mice [9] suggest an action of STARD10 on proinsulin processing in the β-cell. We, therefore, next investigated this hypothesis by performing a metabolic labelling pulse-chase experiment in isolated islets from WT and β*Stard10*KO mice.
After 20 min of pulse-labelling with ^{35}S-amino acids, the islets of both genotypes were chased for 1.5 or 4 h in 5.5 mM glucose medium. Insulin was immunoprecipitated from both the cell lysate (C) and the secretion media (M) (Figure 2A). Labelled proinsulin secretion by β*Stard10*KO islets was increased at low (5.5 mM) glucose compared to *Ctl* mice after 4 h of chase (Figure 2B; *Ctl*: 8.46 ± 2.11 versus β*Stard10*KO: 12.64 ± 2.42% total; $^*P < 0.05$, Mann—Whitney test, $n = 4$—5 animals). This increase in basal proinsulin secretion in the KO islets tended to be observed from 1.5 h of chase (Figure 2B; *Ctl*: 6.60 ± 1.32 versus β*Stard10*KO: 9.58 ± 3.37% total; $P = 0.064$, Mann—Whitney test, $n = 4$—5 animals). The secreted labelled proinsulin:insulin ratio was also increased after 1.5 h of chase (Figure 2C; *Ctl*: 0.85 ± 0.40 versus β*Stard10*KO: 2.05 ± 0.88; $P < 0.05$, Mann—Whitney test, $n = 4$—5 animals), but no apparent change was noted in the labelled proinsulin:insulin ratio inside the cells (Figure 2D; 1.5 h: *Ctl*: 0.29 ± 0.07 versus β*Stard10*KO: 0.27 ± 0.04, 4 h: *Ctl*: 0.17 ± 0.06 versus β*Stard10*KO: 0.16 ± 0.04, ns, Mann—Whitney test, $n = 4$—5 animals) or in the newly synthesised stored insulin remaining in the cells (Figure 2E; 1.5 h: *Ctl*: 0.56 ± 0.09 versus β*Stard10*KO: 0.61 ± 0.07; 4 h: *Ctl*: 0.45 ± 0.15 versus β*Stard10*KO: 0.53 ± 0.07, ns, Mann—Whitney test, $n = 4$—5 animals).
A similar experiment was carried out where the islets were chased after 30 min in 20 mM glucose (Figure 2F). Although the proinsulin

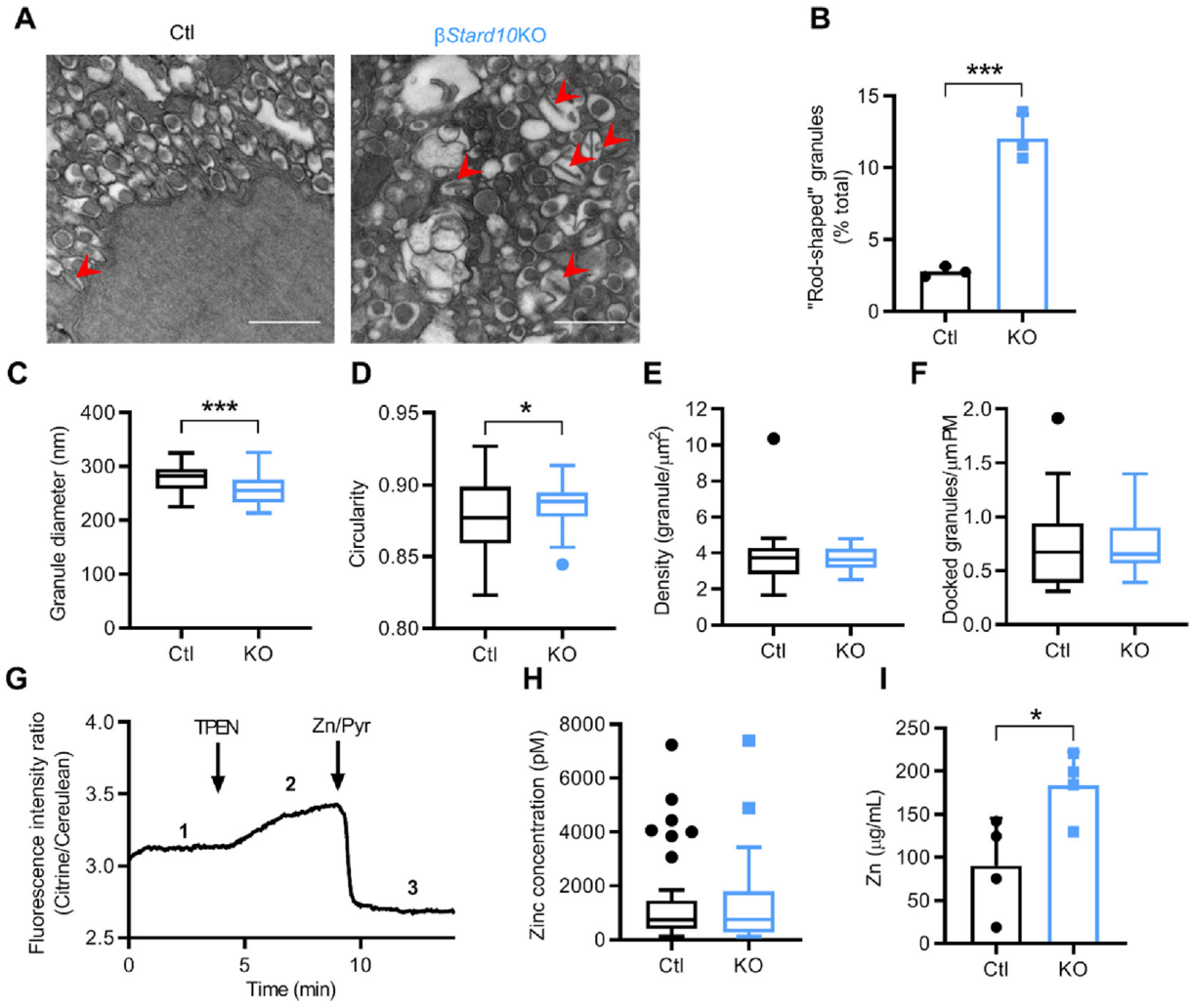

Figure 1: β*Stard10*KO *β-cells display altered granule morphology.* A, Representative Transmission Electron Microscopy images of *control (Ctl)* and β*Stard10*KO β-cells. Red arrowhead: granules with a "rod-shaped" core. Scale bar = 1 μm. B, "Rod-shaped" core granule numbers are increased in the β*Stard10*KO β-cells ($n = 3$ animals, 6 images per animal; $P < 0.001$, Student's *t*-test). C, β-cell granule diameter (nm) ($n = 42$ images from 3 animals, $P < 0.001$, Student's *t*-test). D, β-cell granule "circularity" ($n = 42$ images from 3 animals, $P < 0.05$, Welch's *t*-test). E, β-cell granule density ($n = 19$ images from 3 animals, ns, Mann—Whitney test). F, β-cell morphologically docked granules (per μm plasma membrane) ($n = 18$ images from 3 animals, ns, Mann—Whitney test). G, Representative trace for β-cell expressing the cytosolic eCALWY4 Zn^{2+} sensor. Steady-state fluorescence intensity ratio (citrine/cerulean) (1, R) was first measured before the maximum ratio (2, Rmax) was obtained under perfusion with buffer containing 50 μM TPEN (zinc-free condition). Finally, the minimum ratio (3, Rmin) was obtained under perfusion with buffer containing 5 μM pyrithione and 100 μM Zn^{2+} (zinc-saturated condition). Cytosolic free Zn^{2+} concentrations were calculated using the following formula: (R-Rmin)/(Rmax-Rmin). H, Cytosolic Zn^{2+} concentrations measured by eCALWY4 in *Ctl* and β*Stard10*KO β-cells (n = 33—65 cells per genotype, ns, Mann—Whitney test). I, Total islet zinc measured by inductively coupled plasma mass spectrometry (ICP/MS) in *Ctl* and β*Stard10*KO animals (n = 4 animals/genotype, $*P < 0.05$, unpaired *t*-test).

secretion and the secreted proinsulin:insulin ratio from the KO islets at 20 mM glucose tended to be increased versus wild-type islets, values were not significantly different between genotypes (Figure 2G,H). It is worth noting that insulin granules ordinarily have a long lifespan in β-cells, with a half-life of several days [22], indicating that the labelled peptides observed in this experiment originate from young granules.

In order to determine whether the increase in newly synthesised proinsulin secretion observed in the pulse-chase experiment reflected a change in total secreted proinsulin, we measured the total insulin and proinsulin in the secretion medium after 30 min in low (3 mM) or stimulating (17 mM) glucose concentrations. However, the secreted proinsulin:insulin ratios remained unchanged between genotypes at both glucose concentrations (Figure 2I).

3.4. Preserved glucose-regulated membrane potential and β-cell—β-cell connectivity in Stard10KO islets

Our previous study [9] showed that the deletion of *Stard10* in the β-cell impaired glucose-induced cytoplasmic Ca^{2+} increases and insulin secretion. To test for a potential upstream defect, e.g., in the closure of ATP-sensitive K^+ (K_{ATP}) channels [23], we performed perforated patch-clamp electrophysiology [24] to measure plasma membrane potential in dispersed single β-cells. No change in glucose-induced membrane depolarisation was observed in β-cells from β*Stard10*KO animals compared to WT littermates (Supplemental Figures 2A and 2B).

β-cell—β-cell connections are essential for synchronised intraislet Ca^{2+} influx and ultimately efficient insulin secretion [3]. We subjected

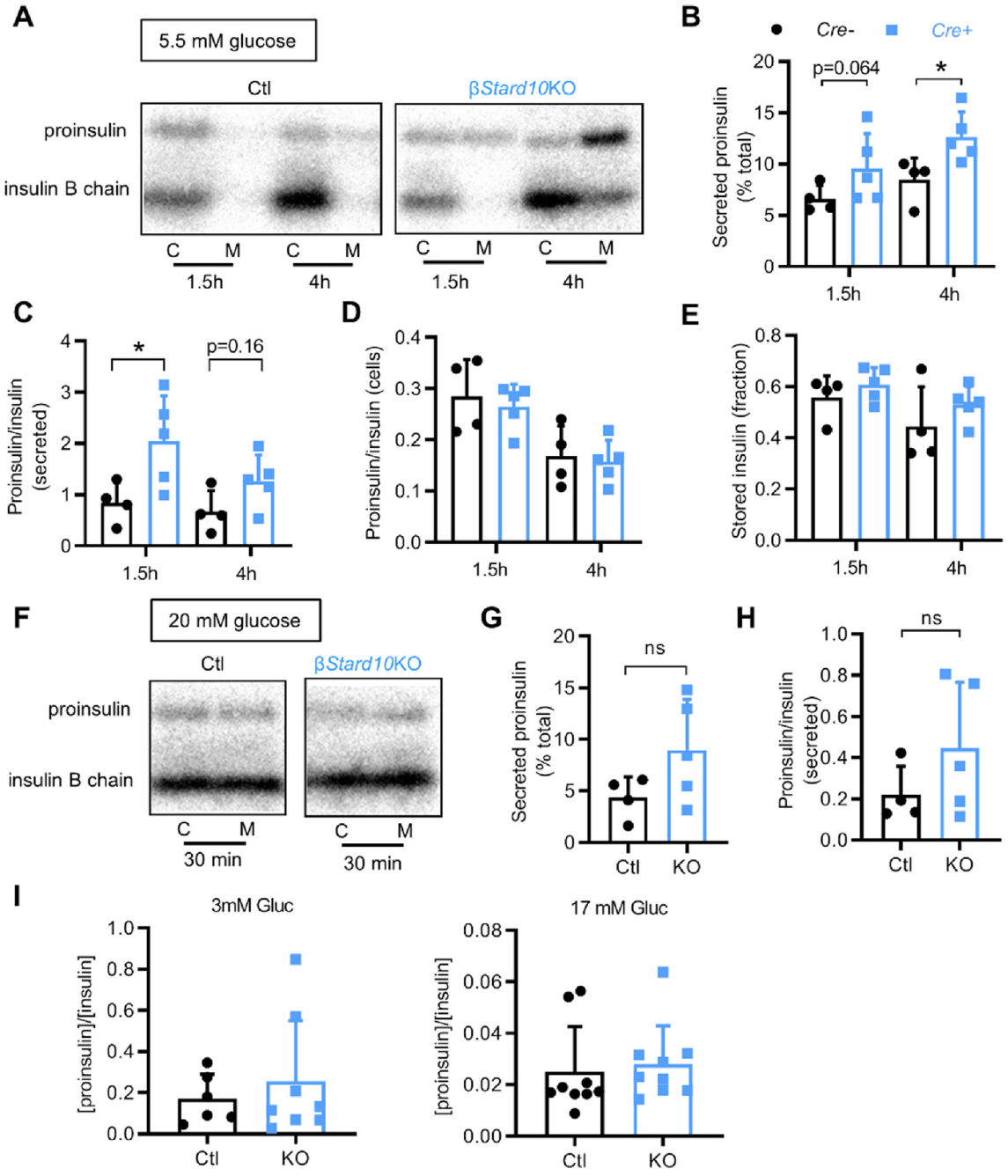

Figure 2: Deletion of *Stard10* increased basal secretion of newly synthesised proinsulin but did not affect total secreted proinsulin:insulin ratio. A, Representative phosphorimages from reducing gels representing ^{35}S-labelled proinsulin and insulin (B chain) originating from cell lysate (C) or secreting medium (M) samples after 1.5 or 4 h of a chase in 5.5 mM glucose medium. B, Secreted proinsulin after 1.5 or 4 h of a chase in 5.5 mM glucose medium expressed as a percentage of total labelled proinsulin ($n = 4–5$ animals; $^*P < 0.05$, Mann–Whitney test). C, Secreted proinsulin:insulin ratio after 1.5 or 4 h of a chase in 5.5 mM glucose medium ($n = 4–5$ animals; $^*P < 0.05$, Mann–Whitney test). D, Fraction of stored processed insulin remaining inside the cells after 1.5 or 4 h of a chase in 5.5 mM glucose medium ($n = 4–5$ animals; ns, Mann–Whitney test). E, Cellular proinsulin:insulin ratio after 1.5 or 4 h of a chase in 5.5 mM glucose medium ($n = 4–5$ animals; ns, Mann–Whitney test). F, Representative phosphorimages from reducing gels representing ^{35}S-labelled proinsulin and insulin (B chain) originating from cell lysate (C) or secreting medium (M) samples after 30 min of a chase in 20 mM glucose medium. G, Secreted proinsulin after 30 min of a chase in 20 mM glucose medium expressed as a percentage of total labelled proinsulin ($n = 4–5$ animals; ns, Mann–Whitney test). H, Secreted proinsulin:insulin ratio after 30 min of a chase in 20 mM glucose medium ($n = 4–5$ animals; ns, Mann–Whitney test). Quantification for B, C, D, E, G, and H was done on the phosphorimages obtained from reducing gels. I, Secreted total proinsulin:insulin ratio after 30 min secretion by isolated islets in 3 or 17 mM glucose Krebs-HEPES-bicarbonate buffer.

the individual Ca^{2+} traces recorded from fluo-2-loaded β-cells in the intact mouse islets to correlation (Pearson R) analysis to map cell—cell connectivity [6,7,25]. In the presence of low (3 mM) glucose, β-cells displayed low levels of coordinated activity in islets of WT and whole body *Stard10*KO animals, as assessed by counting the numbers of coordinated cell pairs (Supplemental Figures 3A and 3B; 21.70 ± 9.13% versus 18.95 ± 17.47% for WT versus KO, respectively, ns). By contrast, β-cells displayed highly coordinated Ca^{2+} responses upon the addition of 17 mM glucose or 20 mM KCl (the latter provoking depolarisation and a synchronised Ca^{2+} peak; not shown) in WT islets. None of the above parameters were altered in KO islets (Supplemental Figures 3A and 3B; 17 mM G: 98.61 ± 1.34% versus 92.23 ± 10.46% for WT versus KO; KCl: 92.63 ± 7.23% versus 93.36 ± 11.44% for WT versus KO, respectively; ns). Similarly, the analysis of correlation strength in the same islets (Supplemental Figures 3C and 3D) revealed no significant differences between genotypes.

3.5. Solution of STARD10 3D structure and molecular docking identify PI and PI(3)P as potential ligands

To assess which membrane lipids may be bound by STARD10, we sought to obtain a crystal structure of the purified protein. We generated and purified the recombinant protein from a bacterial expression construct comprising the human STARD10 coding sequence fused with a 6His-MBP (Maltose Binding Protein) tag. Following the recombinant protein production in *E. coli* and protein purification, STARD10 generated a well-diffracting crystal. The crystal structure was then resolved at 2.3 Å resolution by molecular replacement using the structure of STARD5 (PDB ID: 2R55) (Figure 3A; Supplemental Movie 1; Supplemental Table 2).

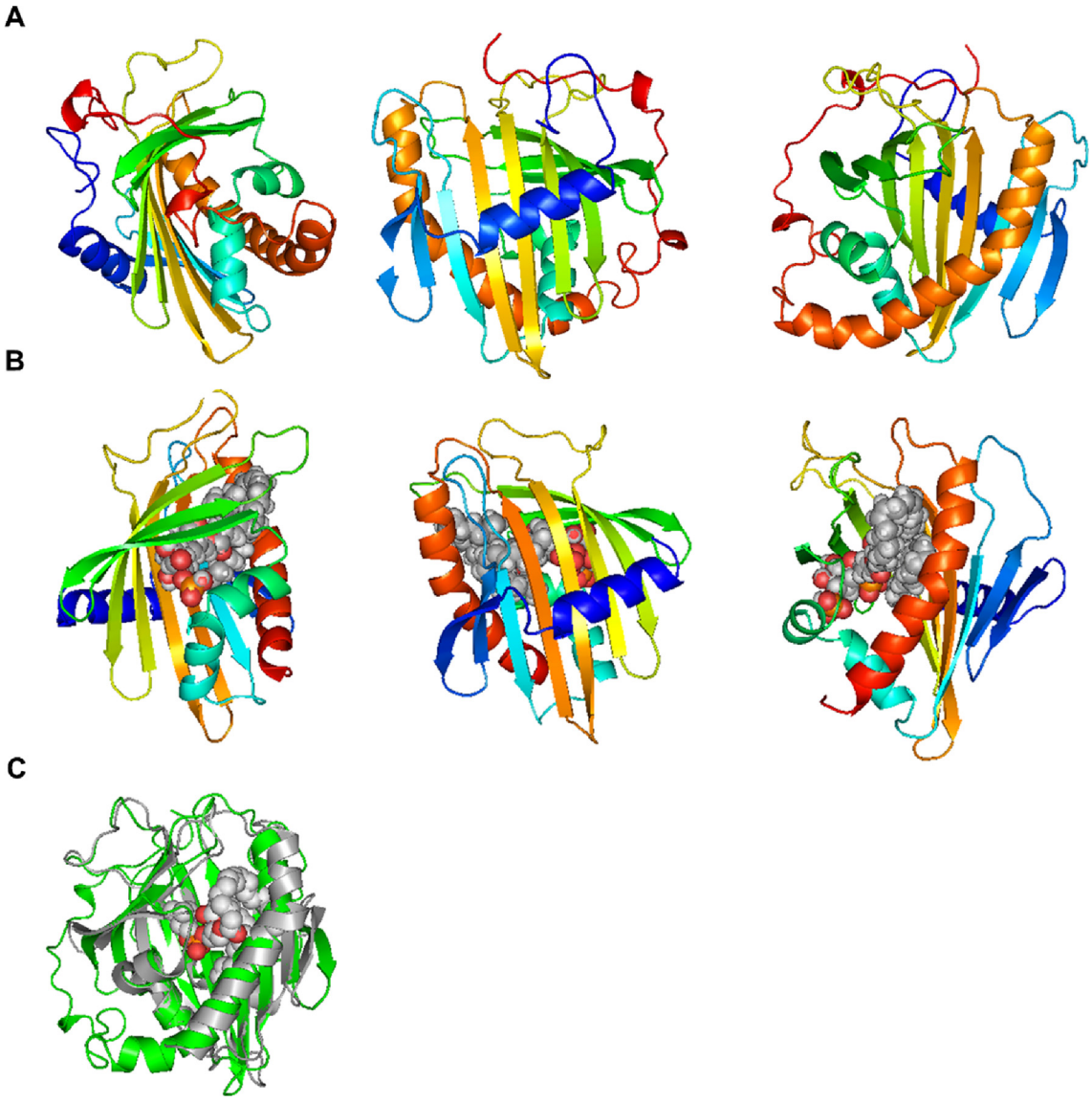

Figure 3: *Structure of H. sapiens STARD10.* A, Three-dimensional views at 2.3 Å of the crystal structure of unliganded human STARD10: ribbon diagram coloured from the N-terminus (blue) to the C-terminus (red). B, Docking of phosphatidyl-inositol 3 phosphate (PI(3)P) to the human STARD10 structure. STARD10 cavity is larger than the phosphatidylcholine transporter protein STARD2 and, contrary to the latter, readily accommodates phosphatidylinositols. The three projections shown in A and B are rotated by 120° with respect to each other. C, Comparison of unliganded STARD10 (green) and its close family relative STARD2 (grey) bound to phosphatidylcholine.

Supplementary video related to this article can be found at https://doi.org/10.1016/j.molmet.2020.101015

In the STARD10 crystal structure, the dimensions of the cavity are such that the protein is expected to readily accommodate phosphatidylinositols, whereas the equivalent STARD2 cavity, due to its smaller size, gives a poor predicted binding energy. On this basis, the STARD10 binding pocket is expected to bind PI and various phosphorylated PIs with higher affinity than STARD2.

To test this prediction, the head groups of PI and PI(3)P (glycero-inositol-1-phosphate and glycero-3-phosphoinositol-1-phosphate) were docked into the 3-dimensional structure of STARD10 (described above) and the closest family member STARD2 [26] by using the BUDE [27] (Figure 3B, Supplemental Movie 2). The software was used to dock different representative conformations of the ligand to the target protein: 87 conformers for PI and 85 for PI(3)P. When these conformers were docked to STARD10, all final poses were located inside the binding cavity. On the other hand, for STARD2, only two conformers were placed by BUDE inside the protein, and the rest were docked onto the outer surface of the protein, suggesting that, contrary to STARD10, binding inside STARD2 by PI and PI(3)P is unfavourable. Likewise, the predicted binding energies of the PI and PI(3)P head groups to STARD10 are about 40 kJ mol^{-1} better than those to STARD2 (Figure 3C presents a comparison between STARD10 (unliganded, in green) and STARD2 (bound to phosphatidylcholine, in grey)).

Supplementary video related to this article can be found at https://doi.org/10.1016/j.molmet.2020.101015

3.6. STARD10 binds to phosphatidylinositides

In order to confirm the above inferences based on the STARD10 structure and molecular docking, we performed a lipid overlay assay, in which *in vitro* lipid binding to a range of phospholipids spotted onto a nitrocellulose membrane is assessed [28]. The efficiency and specificity of protein purification were monitored by SDS-PAGE staining with Coomassie Blue (Figure 4A). Purified STARD10 protein was incubated with the PIP membrane strips and detected using an anti-STARD10 antibody and secondary anti-goat-HRP antibody (Figure 4B). Interestingly, STARD10 interacted with all PIP species interrogated, suggesting that STARD10 may bind to membranes containing these phospholipids.

3.7. Altered lipidomic profile in βStard10KO islets

The above observations suggested that the loss of lipid binding (including phosphoinositides) and transport by STARD10 in β*Stard10*KO cells might result in changes in granule or cellular lipid composition which in turn may affect granule biogenesis (Figure 1A). Since granule lipids could not readily be quantified given the relatively small numbers of β-cells that can usually be isolated from the mouse pancreas (~200 000, or ~20 μg protein), precluding granule isolation at the scale needed, we limited our studies to whole islets. The lipid composition of Ctl and *Stard10*-null β-cells was explored by targeted mass spectrometry. Of 24 classes and 280 species of lipids measured (Supplemental Table 3), total cholesteryl esters (*Ctl*: 1.60 ± 0.36 versus β*Stard10*KO: 2.24 ± 0.50% total lipids; $^{**}P < 0.01$, paired *t*-test) and phosphatidylinositols (PIs) (*Ctl*: 7.63 ± 1.15 versus β*Stard10*KO: 8.98 ± 1.16% total lipids; $^{*}P < 0.05$, paired *t*-test) as well as a particular species of phosphatidylethanolamine (PE 34:0; *Ctl*: 0.019 ± 0.0029 versus β*Stard10*KO: 0.024 ± 0.0022% total lipids; $^{*}P < 0.05$, paired *t*-test) were all significantly increased in the KO islets versus *Ctl* (Figure 5), suggesting that STARD10 is involved in the regulation of the turnover of these lipid species.

3.8. STARD10 is localised to the cytoplasm and nucleus of the β-cell

As an alternative approach to address which intracellular membranes may be affected by alterations in STARD10 expression, and hence lipid distribution, we next performed a confocal analysis of the subcellular localisation of STARD10. In the absence of a commercial antibody able to detect endogenous STARD10 by immunocytochemistry, we over-expressed the protein tagged with the GFP either in carboxy- or amino-terminus in the human β-cell line EndoC-βH1 [29]. STARD10 was present homogenously in the cytosol and nucleus, and we saw no particular localisation to a given organelle or membrane (Figure 6).

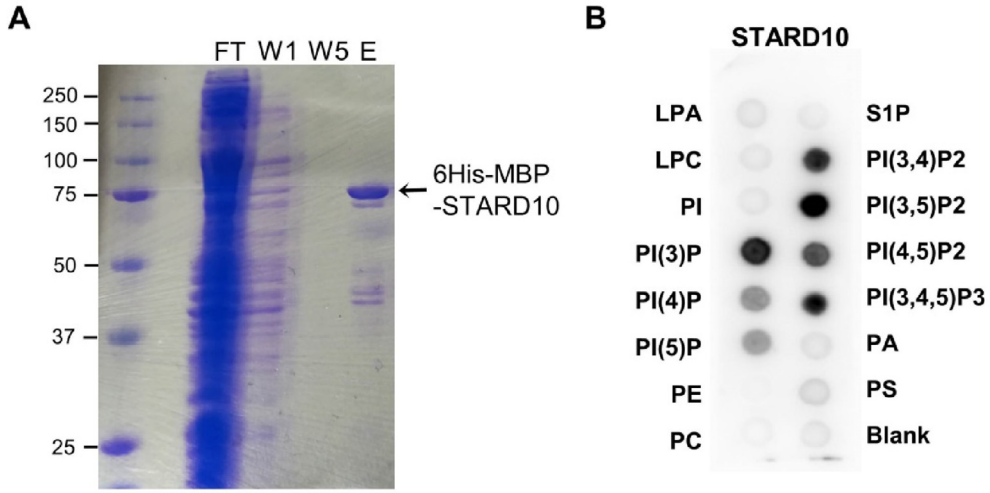

Figure 4: *Phosphoinositide binding to STARD10.* A, Coomassie blue staining of 6His-MBP-STARD10 (75 kDa) purified by Immobilised Metal Affinity Column (IMAC): FT: flow-through, W1: first column wash, W5: last column wash, E: elution. B, Lipid overlay assay. LPA, lysophosphatidic acid; S1P, sphingosine-1-phosphate; LPC, lysophosphatidylcholine; PI, phosphatidylinositol; PI(3)P, PI-(3)-phosphate; PI(4)P, PI-(4)-phosphate; PI(5)P, PI-(5)-phosphate; PE, phosphatidylethanolamine; PC, phosphatidylcholine; $PI(3,4)P_2$, PI-(3,4)-bisphosphate; $PI(3,5)P_2$, PI-(3,5)-bisphosphate; $PI(4,5)P_2$, PI-(4,5)-bisphosphate; $PIP(3,4,5)P_3$, PI-(3,4,5)-trisphosphate; PA, phosphatidic acid; PS, phosphatidylserine. Immunodetection of bound protein was performed using a primary anti-STARD10 antibody (Santa Cruz) and a secondary anti-goat-HRP antibody (Santa Cruz). STARD10 was bound to all PIP species.

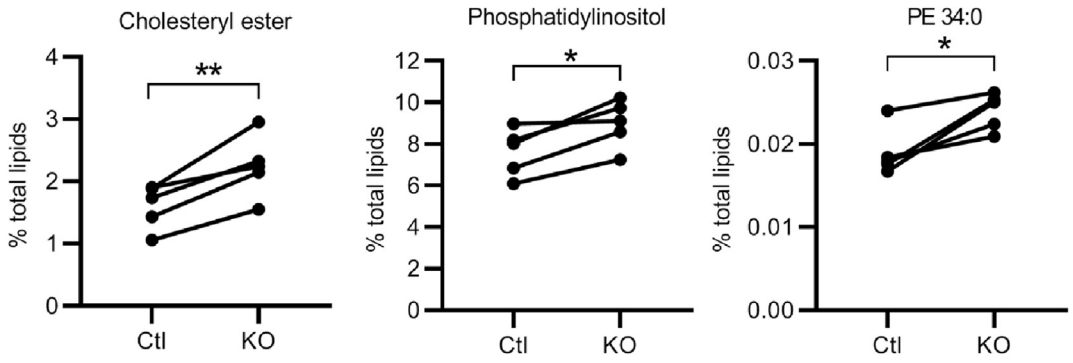

Figure 5: *Altered lipidomic profile in βStard10KO islets.* The deletion of *Stard10* in mouse pancreatic β-cells significantly increased the total cholesteryl esters, phosphatidylinositols, and the phosphatidylethanolamine species 34:0 in islets (n = 5 animals; $^{*}P < 0.05$, $^{**}P < 0.01$, paired *t*-test). See Supplemental Table 3 for a complete list of all the lipids measured.

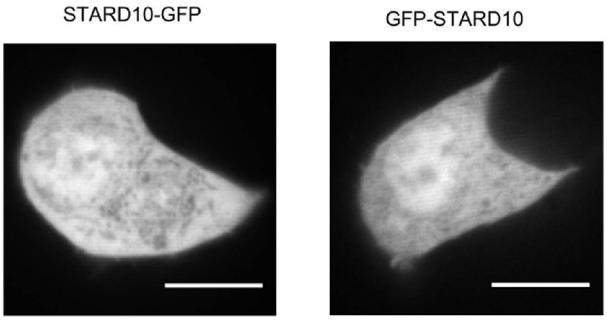

Figure 6: Subcellular localisation of STARD10-GFP (left panel) and GFP-STARD10 (right panel) in EndoC-βH1 cells. Scale bar = 10 μm.

3.9. STARD10 interactome analysis identifies proteins involved in phosphatidylinositide signalling

To gain further insights into the possible mechanisms through which STARD10 may influence granule lipid composition, and other processes pertinent to the control of insulin secretion, protein interacting partners of STARD10 were identified by immunoprecipitation of the endogenous protein in the rat pancreatic β-cell line INS1 (832/13) and liquid chromatography—tandem mass spectrometry analysis after TMT labelling of the digested samples. 303 significantly enriched proteins were detected in the STARD10 pull-down condition compared with the nontargeting control IgG ($P < 0.05$ and FDR<0.05, paired *t*-test) (Table 1). Amongst these significant interactions, we observed proteins well known to play a role in β-cell physiology: the pore-forming subunit Kir6.2 (Kcnj11, ATP-sensitive inward rectifier potassium channel 11) and its auxiliary subunit, the sulfonylurea receptor SUR1 (Abcc8, ATP-binding cassette subfamily C member 8) of the ATP-sensitive K^+ (K_{ATP}) channel [30]; the phosphoinositide $PI(4,5)P_2$-interacting protein granuphilin (Sytl4; synaptotagmin-like 4) associates with and is involved in the docking of the insulin granules [31]; the polypyrimidine tract-binding protein 1 (Ptbp1) is required for the translation of proteins localised in the insulin granule in response to glucose [32]. Gene ontology analysis of the identified STARD10 binding partners reflected an enrichment in proteins associated with RNA binding and processing, gene expression, and splicing (Supplemental Tables 4, 5, and 6). Interestingly, STARD10 also interacted with the inositol lipid kinase phosphatidylinositol 5-phosphate 4-kinase type-2 gamma (Pip4k2c) enzyme, which converts phosphatidylinositol 5-phosphate (PI(5)P) into phosphatidylinositol 4,5-bisphosphate ($PI(4,5)P_2$) [33].

The efficiency and specificity of STARD10 immunoprecipitation by the antibody and the co-immunoprecipitation of the Kir6.2 channel were confirmed by Western (immuno-)blot analysis (Supplemental Figure 4)

3.10. Altered expression of genes controlling inositol phospholipid signalling in βStard10KO islets

STARD10 has previously been reported to influence the activity of peroxisome proliferator-activated factor (PPARα) in the liver [34], suggesting a possible influence on gene expression in the β-cell. In order to assess this possibility, we performed massive parallel RNA sequencing (RNAseq) on islets from WT and β*Stard10*KO mice. We identified 88 differentially regulated genes (*padj*<0.05, $n = 6$ animals), with 33 being upregulated and 55 being downregulated in KO versus WT islets. The list of the 20 most significantly regulated genes is presented in Supplementary Figure 5A and Table 2 (*padj* ranging from 1.71×10^{-157} to 2.25×10^{-3}). As expected, a decrease in *Ins1* expression in the β*Stard10*KO mice carrying an Ins1-*Cre* knock-in allele was observed.

Interestingly, *Scg2*, encoding secretogranin 2, a member of the granin protein family, localised in secretory vesicles [35], and *Rasd2*, also known as Ras homologue enriched in striatum (Rhes), were upregulated. Interestingly, consistent with possible changes in phosphoinositide signalling, *Pirt* (phosphoinositide-interacting regulator of transient receptor potential channels), a regulator of transient receptor potential Ca^{2+} channels [36], and *Syt1* (synaptotagmin 1) regulating fast exocytosis and endocytosis in INS1 cells [37] were downregulated in β*Stard10*KO islets.

Enrichment analysis through the gene ontology consortium website (http://www.geneontology.org/) identified genes whose products are localised in neuronal projections (11 genes, fold enrichment = 4.57, $P < 0.05$) and neurons (12 genes, fold enrichment = 3.95, $P < 0.05$) amongst the downregulated genes (Supplemental Figure 5B, Supplemental Table 7). As secretory cells, neurons share their transport and secretory machinery with β-cells, suggesting that these genes play a role in the insulin secretion process. Amongst the genes identified, several are implicated in insulin secretion and/or β-cell survival: *Chl1* (cell adhesion molecule L1-like), whose silencing has previously been shown to reduce glucose-induced insulin secretion in INS1 cells [38] and is downregulated in islets from type 2 diabetic subjects [39]; *Nos1* (neuronal nitric oxide synthase), implicated in insulin secretion and β-cell survival [40]; *Adcyap1r1* (adenylate cyclase-activating polypeptide 1 receptor 1), encoding the PAC1 receptor of the pituitary adenylate cyclase-activating polypeptide (PACAP)

Table 1 — *STARD10 binding partners identified by mass spectrometry in INS1 (832/13) cells.* 20 most significantly enriched proteins were found in the STARD10 pull-down condition versus control IgG with a cut-off of at least 5 unique peptides identified.

Accession	Gene symbol	log2 Fold Change	FDR	Protein name
G3V702	Smu1	4.1143	0.002426	Smu-1 suppressor of mec-8 and unc-52 homologue (*C. elegans*)
Q56A27	Ncbp1	4.4449	0.002435	Nuclear cap-binding protein subunit 1
Q63570	Psmc4	3.7556	0.006621	26S proteasome regulatory subunit 6B
F1LX68	Spats2	4.2439	0.006621	Spermatogenesis-associated, serine-rich 2
Q3B8Q1	Ddx21	3.1883	0.006621	Nucleolar RNA helicase 2
A0A0G2QC21	Arhgef7	5.1017	0.006621	Rho guanine nucleotide exchange factor 7
Q5XIW8	Sart1	3.6068	0.006621	U4/U6.U5 tri-snRNP-associated protein 1
Q6AYI1	Ddx5	3.5220	0.006621	DEAD (Asp-Glu-Ala-Asp) box polypeptide 5
P62718	Rpl18a	5.3046	0.006621	60S ribosomal protein L18a
Q4FZT9	Psmd2	5.0539	0.006621	26S proteasome non-ATPase regulatory subunit 2
P62198	Psmc5	5.1616	0.006621	26S proteasome regulatory subunit 8
G3V8B6	Psmd1	3.6940	0.006621	26S proteasome non-ATPase regulatory subunit 1
P70673	Kcnj11	5.1478	0.007165	ATP-sensitive inward rectifier potassium channel 11
Q3B8Q2	Eif4a3	5.3478	0.007229	Eukaryotic initiation factor 4A-III
Q5XIH7	Phb2	4.8776	0.007229	Prohibitin-2
P62193	Psmc1	5.0757	0.007229	26S proteasome regulatory subunit 4
M0R735	Syncrip	5.9137	0.007229	Heterogeneous nuclear ribonucleoprotein Q
A0A0G2JTI7	Prpf3	4.0762	0.007229	Pre-mRNA-processing factor 3
D4A0U3	Zfp638	3.6588	0.007229	Zinc finger protein 638
D3ZZR5	Snrpa1	2.4835	0.007229	Small nuclear ribonucleoprotein polypeptide

neuroendocrine factor [41]; and *Cplx1* (complexin 1) [42]. None of several key β-cell signature genes involved in the regulation of *Ins* expression and β-cell identity (Supplemental Figure 5C), or of the "disallowed" β-cell gene family (Supplemental Figure 5D) [3], were affected by *Stard10* deletion.

4. DISCUSSION

Our earlier demonstration [10] that *STARD10* is the likely causal gene at the T2D risk locus on chromosome 11q13 has emphasised the probable importance of lipid transfer for the normal physiology of the pancreatic β-cell. Indeed, the role of lipid transfer proteins has emerged recently as an important element in cell biology [43].

Several lines of evidence presented in our studies support a role for STARD10 in PI/PIPs binding and potentially transport between intracellular membranes. (a) Resolution of the crystal structure of STARD10 and molecular docking predict the binding of PI/PIPs in its binding pocket (Figure 3). (b) Purified recombinant STARD10 binds to phosphatidylinositide species in a lipid overlay assay (Figure 4). (c) The phosphatidylinositol content was increased in βStard10KO compared to control islets (Figure 5). (d) Our proteomic study identified the phosphatidylinositol 5-phosphate 4-kinase type-2 gamma (Pip4k2c) enzyme and the PI(4,5)P_2-binding protein granuphilin [44] as STARD10 binding partners. (e) The expression of the phosphoinositide-binding proteins *Syt1* and *Pirt* were decreased in β*Stard10*KO islets (Supplemental Figure 5). *Pirt* encodes a phosphoinositide-interacting regulator of the transient receptor potential (TRP) Ca^{2+} channels. Several TRP channels are expressed in the β-cell and an increasing number of data points towards the role of these channels in the regulation of insulin secretion [45]. A previous study [46] has shown that female *Pirt*$^{-/-}$ mice are heavier than controls and develop glucose intolerance.

Table 2 — *RNA seq identification of differentially regulated genes in βStard10KO islets.* 20 first differentially regulated genes in *βStard10KO* were ranked by increasing adjusted *P* value (*padj*) with their relative expression versus WT (log2 fold change).

	symbol	log2 Fold Change	*P* value	*padj*	entrezID
ENSMUSG00000030688	Stard10	−1.3455	1.13E-161	1.71E-157	56018
ENSMUSG00000035804	Ins1	−0.5451	1.46E-17	1.11E-13	16333
ENSMUSG00000050711	Scg2	0.2439	2.13E-13	1.07E-09	20254
ENSMUSG00000043639	Rbm20	0.4753	3.35E-12	1.27E-08	73713
ENSMUSG00000028989	Angptl7	0.4761	1.40E-10	4.23E-07	654812
ENSMUSG00000034472	Rasd2	0.4568	2.99E-10	7.52E-07	75141
ENSMUSG00000048070	Pirt	−0.4203	1.71E-09	3.68E-06	193003
ENSMUSG00000038112	AW551984	−0.3837	5.31E-09	1.00E-05	244810
ENSMUSG00000000386	Mx1	0.4094	3.87E-08	6.49E-05	17857
ENSMUSG00000019189	Rnf145	0.1714	1.22E-07	0.000185	74315
ENSMUSG00000025085	Ablim1	0.2650	1.69E-07	0.000232	226251
ENSMUSG00000007946	Phox2a	−0.3054	2.01E-07	0.000253	11859
ENSMUSG00000032269	Htr3a	−0.3423	2.37E-07	0.000276	15561
ENSMUSG00000029361	Nos1	−0.3533	4.34E-07	0.000468	18125
ENSMUSG00000092035	Peg10	−0.2823	8.04E-07	0.00081	170676
ENSMUSG00000051855	Mest	−0.3041	1.06E-06	0.000999	17294
ENSMUSG00000025348	Itga7	−0.3500	1.38E-06	0.001223	16404
ENSMUSG00000029219	Slc10a4	−0.2939	1.53E-06	0.00128	231290
ENSMUSG00000034981	Parm1	−0.3002	1.89E-06	0.001502	231440
ENSMUSG00000060519	Tor3a	0.1692	2.98E-06	0.002254	30935

Taken together, these data suggest that STARD10 may bind PI and/or PIPs either in the lipid-binding pocket, as predicted by the crystal structure and molecular docking (Figure 3), or at the surface of the protein. We note that the findings from the lipid overlay assay are consistent with a binding of STARD10 to membranes containing PIP lipids (with an affinity which appears higher for (3)P containing species). This could be important for the targeting of STARD10 to specific membrane compartments. In contrast to its closest relative STARD2, which has been shown to selectively bind phosphatidylcholine [47], our crystal structure determination and molecular docking indicate that STARD10, due to its larger binding pocket, is predicted to bind phosphatidylinositol (PI) and its various phosphorylated forms (PIPs) (Figure 3) in addition to its previously recognised ligands phosphatidylcholine and phosphatidylethanolamine [11].

Consistent with likely mistargeting of lipids to membranes involved in insulin secretion, we demonstrate that STARD10 is required for normal secretory granule maturation in murine β-cells. Of note, recent findings [48] have indicated that cholesterol is also required for normal granule maturation. In addition, in INS-1 (832/13) cells, the insulin secretory granule was found to contain a high proportion of phosphatidylinositol (∼20%, 5-fold that in the whole cell) [48]. It is thus conceivable that the changes in secretory granule biogenesis may occur as a result of changes in lipid delivery to the granule membrane and/or transcriptional events (i.e., altered gene expression). In contrast, we were not able to obtain evidence for an effect of STARD10 variation on human β-cell granules, perhaps reflecting a greater diversity in granule structure observed in man, as well as the limited number of subjects available for analysis.

Proteomic analysis of the STARD10 binding partners in INS1(832/13) pancreatic β-cells (Table 1) identified several proteins involved in insulin secretion such as the subunits of the K_{ATP} channel Kir6.2 and SUR1 and the secretory vesicle protein granuphilin, which possesses a C2 domain capable of binding the phosphoinositide PIP_2 [49]. Another binding partner, PTBP1 (polypyrimidine tract-binding protein 1), regulates the translation of insulin granule proteins in response to glucose [32]. The potential regulation by STARD10 of the activity of this protein could conceivably affect granule structure. Given the known function of STARD proteins in lipid transport, it is possible that, in the absence of STARD10, phospholipids are not addressed to the appropriate membranes in cellular subcompartments. It is, thus, conceivable that the altered lipidomic profile might impact the localisation of STARD10 interacting partners and, therefore, alter their function in the β-cell and in insulin secretion.

RNAseq analysis of the transcriptome of WT and *βStard10*KO islets identified differentially expressed genes which are likely to play a role in adult β-cell physiology (Supplemental Figure 5). Of note, in liver, *Stard10* knockout affects the activity of PPARα [34], and it is conceivable that changes in lipid distribution impact lipid-regulated factors such as those in the β-cell. There is also evidence that another Stard family member, STARD2, binds directly to transcription factors [50], so this mechanism is conceivable for STARD10. The gene products of *Syt1* (synaptotagmin 1) and *Cplx1* (complexin 1) are part of the molecular machinery driving vesicle exocytosis and form a tripartite complex with Soluble N-ethylmaleimide sensitive factor Attachment protein Receptor (SNARE) proteins [51]. However, none of these genes are readily linked to a change in insulin crystallisation or granule biogenesis. Importantly, we also identified *Pirt*, a phosphoinositide-interacting regulator of transient receptor potential channels, as a binding partner of STARD10 and thus likely either to sense or to influence phosphoinositides levels in cells. Changes of the product of these genes at the protein level by Western blotting and/or immunocytochemistry would provide additional validation and information and will be the focus of further studies.

We also considered the possibility that altered granule composition may reflect altered intracellular Zn^{2+} levels given that similar changes are observed after the deletion of the gene encoding the Zn^{2+} transporter ZnT8, *Slc30a8* [52]. Thus, the total Zn^{2+} content, likely reflecting intragranular Zn^{2+}, assessed by ICP/MS, was increased in the islets of β*Stard10*KO versus WT mice (Figure 1). The latter appears unlikely to be due to changes in the expression of *ZnT8* (encoded by *Slc30a8*), which we did not observe, but might reflect altered intrinsic activity, or granule recruitment, of ZnT8 due to altered membrane lipid composition [53]. Consistent with this possibility, anionic phosphatidylinositols increase, whereas nonbilayer phospholipids (promoting membrane curvature), lysophosphatidylcholine (LPC) and phosphatidylethanolamine (PE), lower ZnT8 activity [53].

An unexpected finding from the current study is that β*Stard10*KO islets secreted more radiolabeled proinsulin versus WT after 4 h of a chase in 5.5 mM glucose medium, whilst no difference was observed between genotypes at 20 mM glucose. These results contrast with a *decrease* in the proinsulin:insulin ratio observed in plasma from β*Stard10*KO mice [9] and a similarly lowered ratio in human risk variant carriers versus controls [21]. One possible explanation is that increased proinsulin secretion in unstimulated cells may enrich, for the storage of mature, processed insulin, hence producing a lowered proinsulin:insulin release during stimulation with high glucose. According to studies using radioactive labelling [54] or live-cell imaging of a SNAP-tag fused with insulin [55], young, newly synthesised insulin granules are preferentially secreted upon glucose stimulation. Given their reduced transit time, the proportion of unprocessed proinsulin in the young granules could be higher than that in the older ones. Other evidence points towards the existence of vesicular trafficking pathways leading to unstimulated, "constitutive-like" secretion of proinsulin [56]. It has been speculated [57] that this involves routing to the endosomal compartment and either cargo degradation in the lysosome or secretion at the plasma membrane through a "constitutive-like" pathway [58]. By changing the lipid composition of granules, STARD10 may modulate their trafficking properties, affect the age of secreted granules, and/or decrease their targeting to the lysosomes.

On the other hand, the total proinsulin:insulin ratio in the secretion medium of isolated islets remained unchanged between the two genotypes (Figure 2I), and the cellular (total immunoreactive) proinsulin:insulin ratios were similar in WT and β*Stard10*KO islets (Figure 2D). In addition to its role in insulin crystallisation in dense core granules, zinc ions, which are cosecreted with insulin, inhibit insulin secretion in an autocrine and paracrine manner [59], at least in part through the activation of the pancreatic K_{ATP} channel [60,61]. Zn^{2+} coreleased with insulin also attenuates insulin hepatic clearance, an effect that has been proposed to be mediated through the inhibition of the clathrin-mediated insulin receptor endocytosis by the liver [59]. An increase in Zn^{2+} secretion by the β-cell in the presence of a reduced *STARD10* expression could, thus, participate in the decrease both in insulin secretion and in the plasma proinsulin:insulin ratio observed in the β*Stard10*KO mice [9] and the carriers of the risk alleles [21,62].

A striking finding of our studies is the change in lipid composition observed in the β*Stard10*KO islets (Figure 5). The increased levels of cholesterol, phosphatidylinositol, and PE 34:0 observed may be explained by less efficient transport of lipids, their precursors, or breakdown products between sites of synthesis and degradation in the absence of *Stard10.* Although it was not possible to assess which intracellular membranes may be affected given the limited sensitivity

of the bulk analysis performed and study of changes in lipid profiles in subcompartments such as insulin granule being limited in mouse islet due to the small amount of material compared with cultured cell lines, previous studies have made a link between cholesterol and insulin granule biogenesis and secretion. For example, according to Bogan et al. [63], insulin granules are the major site of cholesterol accumulation inside the β-cell. An excess of cholesterol altered the granule ultrastructure with an increase in mean granule diameter and the retention of immature granule proteins to the granule, changes associated with impaired insulin secretion. In addition, loss of the cholesterol transporter ABCG1from the β-cell led to a decrease in the cholesterol content of the granules and was associated with abnormal, enlarged insulin granules [64].

The impact of altering β-cell cholesterol content and homeostasis, leading to an excess or deficiency in cellular cholesterol content, has previously been achieved through various means, including exogenous addition of cholesterol [65], targeting either cholesterol transporters [48,66,67] or biosynthetic enzymes [68], or the use of an ApoE-deficient mice model [69]. Impaired glucose-induced insulin secretion was observed in all of these cases.

In addition to cholesterol, the insulin secretory granule was found to contain a high proportion of phosphatidylinositol (∼20%, 5-fold that in the whole cell) in INS-1 (832/13) cells [70]. Phosphatidylinositol transfer protein has been shown to increase secretory vesicle formation [71]. Interestingly, the phosphoinositide PI(4)P is present at the granule membrane and its dephosphorylation into PI by the phosphatase Sac 2 is required for efficient insulin secretion by the β-cell [72]. The synthesis of another phosphoinositide, PI(3)P, occurs on secretory vesicles in neurosecretory cells [73], and the inhibition of class II phosphoinositide 3 kinase responsible for the synthesis of PI(3)P from PI impaired insulin secretion [74]. Several additional studies have pointed to the role of phosphoinositides in insulin secretion [75–77].

Moreover, a connection between cholesterol and phosphoinositides in cellular processes has previously been suggested. For example, cholesterol stabilizes phosphoinositide domains, increasing the recruitment of target proteins to the PIP domains [78], and transport proteins with dual phosphoinositide/cholesterol ligands play an important role in the cellular localisation of these lipids [48,79]. In β-cells, cholesterol regulates insulin secretion through $PI(4,5)P_2$ [65].

In addition, the PI transporter TMEM24 regulates pulsatile insulin secretion by replenishing the phosphoinositide pool at the endoplasmic reticulum-plasma membrane contact sites [80]. It is, thus, tempting to speculate that STARD10 might affect insulin secretion in a similar fashion.

In conclusion, we identify phosphatidylinositols as potential new ligands for STARD10. Changes in *STARD10* expression in carriers of type 2 diabetes risk alleles may consequently affect the β-cell lipid composition and alter granule maturation and, ultimately, insulin synthesis and secretion.

AUTHORS' CONTRIBUTIONS

G.R.C. designed and conducted the *in vitro* studies and contributed to the writing of the manuscript. E.H. performed the electrophysiology studies. L.H. and P.A. performed the pulse-chase studies and contributed to the discussion. A.T., A.F. A.K. A.M., and M.S. contributed to the electron microscopy studies. A.P. performed the immunocytochemistry studies. K.C., M.H., and D.B.W. produced STARD10 recombinant protein and performed the structural studies. T.J.P. performed the analyses of the RNAseq data. E.G., T.S., D.J.H., L.J.B. V.S., and W.D. contributed to the connectivity analysis. N.S.A., P.I.B., F.T., and A.K.K.T. performed the lipidomic analysis. K.J.H and P.A.L. performed the interactome analysis. R.B.S. performed the STARD10 ligand docking studies. F.A. provided the STARD10-GFP and GFP-STARD10 constructs. A.C. performed the ICP/MS analysis. I.L. was the holder of the Home Office project licence and responsible for the work carried on animals in this study. G.A.R. conceived the study and cowrote the manuscript. G.A.R. is the guarantor of this work and, as such, had full access to all the data in the study and takes responsibility for the integrity of the data and the accuracy of the data analysis.

FUNDING

G.A.R. was supported by a Wellcome Trust Senior Investigator Award (WT098424AIA) and Investigator Award (212625/Z/18/Z), MRC Programme grants (MR/R022259/1, MR/J0003042/1, and MR/L020149/1) and Experimental Challenge Grant (DIVA, MR/L02036X/1), MRC (MR/N00275X/1), Diabetes UK (BDA/11/0004210, BDA/15/0005275, and BDA 16/0005485) and Imperial Confidence in Concept (ICiC) grants, and a Royal Society Wolfson Research Merit Award. P.A. and L.H. were supported by the NIH (NIH R01 DK48280). I.L. was supported by Diabetes UK Project Grant 16/0005485 and D.J.H. by a Diabetes UK R.D. Lawrence (12/0004431) Fellowship, a Wellcome Trust Institutional Support Award, and MRC (MR/N00275X/1) and Diabetes UK (17/0005681) Project Grants. This project has received funding from the European Research Council (ERC) under the European Union's Horizon 2020 research and innovation programme (Starting Grant 715884 to D.J.H.) and from the Innovative Medicines Initiative 2 Joint Undertaking under grant agreement No. 115881 (RHAPSODY) to G.A.R. and M.S. This Joint Undertaking receives support from the European Union's Horizon 2020 research and innovation programme and EFPIA. A.T. was supported by a project grant from the MRC (MR/R010676/1). V.S. is supported by a Diabetes UK Harry Keen Clinician Scientist 15/0005317. D.W. was supported by the Medical Research Council and Cancer Research UK. The X-ray Crystallography Facility at Imperial College London is partly funded by the Wellcome Trust. The Facility for Imaging by Light Microscopy (FILM) at the Imperial College London is partly supported by funding from the Wellcome Trust (grant 104931/Z/14/Z) and BBSRC (grant BB/L015129/1). The London Metallomics Facility was funded by a Wellcome Trust Multi-User Equipment Grant (202902/Z/16/Z). M.S. was supported by funds from the German Ministry for Education and Research (BMBF) to the German Centre for Diabetes Research (DZD). N.S.A. was supported by the NUS Research Scholarship. A.K.K.T. was supported by the Institute of Molecular and Cell Biology (IMCB), A*STAR.

STUDY APPROVAL

All in vivo procedures were approved by the UK Home Office according to Animals (Scientific Procedures) Act 1986 (HO Licence PPL 70/7349) and were performed at the Central Biomedical Service, Imperial College, London, UK.

Pancreatectomised patient samples were from the IMIDIA consortium (www.imidia.org; Solimena, M, personal communication) with appropriate permissions from donors and/or families and approval by the local ethics committee. A written informed consent was received from participants prior to the inclusion in the study.

DATA AND RESOURCE AVAILABILITY

The RNAseq raw sequence data on βStard10KO and WT mice will be made available via deposition to ArrayExpress.

Lipidomic mass spectrometry raw data can be provided upon request and will be deposited in MetaboLights.
The resources generated or analysed during the current study are available from the corresponding author upon reasonable request.

ACKNOWLEDGMENTS

The authors are grateful to Thomas Di Mattia and Laetitia Voilquin from the Institut de Génétique et de Biologie Moléculaire et Cellulaire (IGBMC), France, for the construction of the STARD10-GFP and GFP-STARD10 plasmids. We thank Rhodri M. L. Morgan for assistance with data collection for the determination of the STARD10 structure, and we acknowledge the Diamond Light Source for access to beamlines I03. We would like to thank the Electron Microscopy Facility of the MPI-CBG for their support. This work was supported by the Electron Microscopy and Histology Facility, a Core Facility of the CMCB Technology Platform at TU Dresden.

CONFLICTS OF INTEREST

G.A.R has received research funding and is a consultant for Sun Pharmaceuticals. He has also received research funding from Servier.

APPENDIX A. SUPPLEMENTARY DATA

Supplementary data to this article can be found online at https://doi.org/10.1016/j.molmet.2020.101015.

REFERENCES

[1] Dodson, G., Steiner, D., 1998. The role of assembly in insulin's biosynthesis. Current Opinion in Structural Biology 8(2):189–194. https://doi.org/10.1016/S0959-440X(98)80037-7.

[2] Rutter, G.A., Pullen, T.J., Hodson, D.J., Martinez-Sanchez, A., 2015. Pancreatic β-cell identity, glucose sensing and the control of insulin secretion. Biochemical Journal 466(2):203–218. https://doi.org/10.1042/BJ20141384.

[3] Rutter, G.A., Hodson, D.J., 2015. Beta cell connectivity in pancreatic islets: a type 2 diabetes target? Cellular and Molecular Life Sciences 72(3):453–467 https://doi.org/10.1007/s00018-014-1755-4.

[4] Rutter, G.A., Hodson, D.J., Chabosseau, P., Haythorne, E., Pullen, T.J., Leclerc, I., 2017. Local and regional control of calcium dynamics in the pancreatic islet. Diabetes, Obesity and Metabolism 19:30–41. https://doi.org/10.1111/dom.12990.

[5] Johnston, N.R., Mitchell, R.K., Haythorne, E., Pessoa, M.P., Semplici, F., Ferrer, J., et al., 2016. Beta cell hubs dictate pancreatic islet responses to glucose. Cell Metabolism 24(3):389–401. https://doi.org/10.1016/j.cmet.2016.06.020.

[6] Hodson, D.J., Mitchell, R.K., Bellomo, E.A., Sun, G., Vinet, L., Meda, P., et al., 2013. Lipotoxicity disrupts incretin-regulated human β cell connectivity. Journal of Clinical Investigation 123(10):4182–4194. https://doi.org/10.1172/JCI68459.

[7] Hodson, D.J., Mitchell, R.K., Marselli, L., Pullen, T.J., Gimeno Brias, S., Semplici, F., et al., 2014. ADCY5 couples glucose to insulin secretion in human islets. Diabetes 63(9):3009–3021. https://doi.org/10.2337/db13-1607.

[8] Mitchell, R.K., Mondragon, A., Chen, L., Mcginty, J.A., French, P.M., Ferrer, J., et al., 2015. Selective disruption of Tcf7l2 in the pancreatic β cell impairs secretory function and lowers β cell mass. Human Molecular Genetics 24(5):1390–1399. https://doi.org/10.1093/hmg/ddu553.

[9] Carrat, G.R., Hu, M., Nguyen-Tu, M.-S., Chabosseau, P., Gaulton, K.J., van de Bunt, M., et al., 2017. Decreased STARD10 expression is associated with defective insulin secretion in humans and mice. The American Journal of Human Genetics 100(2):238–256. https://doi.org/10.1016/j.ajhg.2017.01.011.

[10] Udler, M.S., Kim, J., von Grotthuss, M., Bonàs-Guarch, S., Cole, J.B., Chiou, J., et al., 2018. Type 2 diabetes genetic loci informed by multi-trait associations point to disease mechanisms and subtypes: a soft clustering analysis. PLoS Medicine 15(9). https://doi.org/10.1371/journal.pmed.1002654.

[11] Olayioye, M.A., Vehring, S., Müller, P., Herrmann, A., Schiller, J., Thiele, C., et al., 2005. StarD10, a START domain protein overexpressed in breast cancer, functions as a phospholipid transfer protein. Journal of Biological Chemistry 280(29):27436–27442. https://doi.org/10.1074/jbc.M413330200.

[12] Ravier, M.A., Rutter, G.A., 2010. Isolation and culture of mouse pancreatic islets for ex vivo imaging studies with trappable or recombinant fluorescent probes. Mouse cell culture. Humana Press. p. 171–84.

[13] Chabosseau, P., Tuncay, E., Meur, G., Bellomo, E.A., Hessels, A., Hughes, S., et al., 2014. Mitochondrial and ER-targeted eCALWY probes reveal high levels of free Zn2+. ACS Chemical Biology 9(9):2111–2120 https://doi.org/10.1021/cb5004064.

[14] Schneider, C.A., Rasband, W.S., Eliceiri, K.W., 2012. NIH image to ImageJ: 25 years of image analysis. Nature Methods 9(7):671–675.

[15] Winter, G., Lobley, C.M.C., Prince, S.M., 2013. Decision making in xia2. Acta Crystallographica Section D Biological Crystallography 69(Pt 7):1260–1273. https://doi.org/10.1107/S0907444913015308.

[16] Murshudov, G.N., Vagin, A.A., Dodson, E.J., 1997. Refinement of macromolecular structures by the maximum-likelihood method. Acta Crystallographica Section D Biological Crystallography 53(Pt 3):240–255. https://doi.org/10.1107/S0907444996012255.

[17] Adams, P.D., Afonine, P.V., Bunkóczi, G., Chen, V.B., Davis, I.W., Echols, N., et al., 2010. PHENIX: a comprehensive Python-based system for macromolecular structure solution. Acta Crystallographica Section D Biological Crystallography 66(Pt 2):213–221. https://doi.org/10.1107/S0907444909052925.

[18] Emsley, P., Lohkamp, B., Scott, W.G., Cowtan, K., 2010. Features and development of coot. Acta Crystallographica Section D Biological Crystallography 66(Pt 4):486–501. https://doi.org/10.1107/S0907444910007493.

[19] Brouwers, B., de Faudeur, G., Osipovich, A.B., Goyvaerts, L., Lemaire, K., Boesmans, L., et al., 2014. Impaired islet function in commonly used transgenic mouse lines due to human growth hormone minigene expression. Cell Metabolism 20(6):979–990. https://doi.org/10.1016/j.cmet.2014.11.004.

[20] Lemaire, K., Ravier, M.A., Schraenen, A., Creemers, J.W.M., Plas, R.V. de., Granvik, M., et al., 2009. Insulin crystallization depends on zinc transporter ZnT8 expression, but is not required for normal glucose homeostasis in mice. Proceedings of the National Academy of Sciences 106(35):14872–14877. https://doi.org/10.1073/pnas.0906587106.

[21] Strawbridge, R.J., Dupuis, J., Prokopenko, I., Barker, A., Ahlqvist, E., Rybin, D., et al., 2011. Genome-wide association identifies nine common variants associated with fasting proinsulin levels and provides new insights into the pathophysiology of type 2 diabetes. Diabetes 60(10):2624–2634. https://doi.org/10.2337/db11-0415.

[22] Müller, A., Neukam, M., Ivanova, A., Sönmez, A., Münster, C., Kretschmar, S., et al., 2017. A global approach for quantitative super resolution and electron microscopy on cryo and epoxy sections using self-labeling protein tags. Scientific Reports 7(1):23. https://doi.org/10.1038/s41598-017-00033-x.

[23] Zhang, Q., Ramracheya, R., Lahmann, C., Tarasov, A., Bengtsson, M., Braha, O., et al., 2013. Role of KATP channels in glucose-regulated glucagon secretion and impaired counterregulation in type 2 diabetes. Cell Metabolism 18(6):871–882. https://doi.org/10.1016/j.cmet.2013.10.014.

[24] Tarasov, A.I., Semplici, F., Ravier, M.A., Bellomo, E.A., Pullen, T.J., Gilon, P., et al., 2012. The mitochondrial Ca2+ uniporter MCU is essential for glucose-induced ATP increases in pancreatic β-cells. PloS One 7(7):e39722. https://doi.org/10.1371/journal.pone.0039722.

[25] Hodson, D.J., Schaeffer, M., Romanò, N., Fontanaud, P., Lafont, C., Birkenstock, J., et al., 2012. Existence of long-lasting experience-dependent plasticity in endocrine cell networks. Nature Communications 3:ncomms1612. https://doi.org/10.1038/ncomms1612.

[26] Roderick, S.L., Chan, W.W., Agate, D.S., Olsen, L.R., Vetting, M.W., Rajashankar, K.R., et al., 2002. Structure of human phosphatidylcholine transfer protein in complex with its ligand. Nature Structural & Molecular Biology 9(7):507–511. https://doi.org/10.1038/nsb812.

[27] McIntosh-Smith, S., Wilson, T., Ibarra, A.Á., Crisp, J., Sessions, R.B., 2012. Benchmarking energy efficiency, power costs and carbon emissions on heterogeneous systems. The Computer Journal 55(2):192–205. https://doi.org/10.1093/comjnl/bxr091.

[28] Rousseau, A., McEwen, A.G., Poussin-Courmontagne, P., Rognan, D., Nominé, Y., Rio, M.-C., et al., 2013. TRAF4 is a novel phosphoinositide-binding protein modulating tight junctions and favoring cell migration. PLoS Biology 11(12):e1001726. https://doi.org/10.1371/journal.pbio.1001726.

[29] Ravassard, P., Hazhouz, Y., Pechberty, S., Bricout-Neveu, E., Armanet, M., Czernichow, P., et al., 2011. A genetically engineered human pancreatic β cell line exhibiting glucose-inducible insulin secretion. Journal of Clinical Investigation 121(9):3589–3597. https://doi.org/10.1172/JCI58447.

[30] Cook, D.L., Hales, C.N., 1984. Intracellular ATP directly blocks K+ channels in pancreatic B-cells. Nature 311(5983):271–273. https://doi.org/10.1038/311271a0.

[31] Mizuno, K., Fujita, T., Gomi, H., Izumi, T., 2016. Granuphilin exclusively mediates functional granule docking to the plasma membrane. Scientific Reports 6:23909. https://doi.org/10.1038/srep23909.

[32] Knoch, K.-P., Nath-Sain, S., Petzold, A., Schneider, H., Beck, M., Wegbrod, C., et al., 2014. PTBP1 is required for glucose-stimulated cap-independent translation of insulin granule proteins and Coxsackieviruses in beta cells. Molecular Metabolism 3(5):518–530. https://doi.org/10.1016/j.molmet.2014.05.002.

[33] Clarke, J.H., Emson, P.C., Irvine, R.F., 2008. Localization of phosphatidylinositol phosphate kinase IIgamma in kidney to a membrane trafficking compartment within specialized cells of the nephron. American Journal of Physiology - Renal Physiology 295(5):F1422–F1430. https://doi.org/10.1152/ajprenal.90310.2008.

[34] Ito, M., Yamanashi, Y., Toyoda, Y., Izumi-Nakaseko, H., Oda, S., Sugiyama, A., et al., 2013. Disruption of Stard10 gene alters the PPARalpha-mediated bile acid homeostasis. Biochimica et Biophysica Acta 1831(2):459–468. https://doi.org/10.1016/j.bbalip.2012.11.008.

[35] Zhao, E., Zhang, D., Basak, A., Trudeau, V.L., 2009. New insights into granin-derived peptides: evolution and endocrine roles. General and Comparative Endocrinology 164(2):161–174. https://doi.org/10.1016/j.ygcen.2009.01.011.

[36] Kim, A.Y., Tang, Z., Liu, Q., Patel, K.N., Maag, D., Geng, Y., et al., 2008. Pirt, a phosphoinositide-binding protein, functions as a regulatory subunit of TRPV1. Cell 133(3):475–485. https://doi.org/10.1016/j.cell.2008.02.053.

[37] Xiong, X., Zhou, K.-M., Wu, Z.-X., Xu, T., 2006. Silence of synaptotagmin I in INS-1 cells inhibits fast exocytosis and fast endocytosis. Biochemical and Biophysical Research Communications 347(1):76–82. https://doi.org/10.1016/j.bbrc.2006.06.045.

[38] Taneera, J., Lang, S., Sharma, A., Fadista, J., Zhou, Y., Ahlqvist, E., et al., 2012. A systems genetics approach identifies genes and pathways for type 2 diabetes in human islets. Cell Metabolism 16(1):122–134. https://doi.org/10.1016/j.cmet.2012.06.006.

[39] Solimena, M., Schulte, A.M., Marselli, L., Ehehalt, F., Richter, D., Kleeberg, M., et al., 2018. Systems biology of the IMIDIA biobank from organ donors and pancreatectomised patients defines a novel transcriptomic signature of islets from individuals with type 2 diabetes. Diabetologia 61(3):641–657. https://doi.org/10.1007/s00125-017-4500-3.

[40] Kaneko, Y.K., Ishikawa, T., 2013. Dual role of nitric oxide in pancreatic β-cells. Journal of Pharmacological Sciences 123(4):295–300. https://doi.org/10.1254/jphs.13R10CP.

[41] Winzell, M.S., Ahrén, B., 2007. Role of VIP and PACAP in islet function. Peptides 28(9):1805–1813. https://doi.org/10.1016/j.peptides.2007.04.024.

[42] Abderrahmani, A., Niederhauser, G., Plaisance, V., Roehrich, M.-E., Lenain, V., Coppola, T., et al., 2004. Complexin I regulates glucose-induced secretion in pancreatic β-cells. Journal of Cell Science 117(11):2239–2247. https://doi.org/10.1242/jcs.01041.

[43] Wong, L.H., Čopič, A., Levine, T.P., 2017. Advances on the transfer of lipids by lipid transfer proteins. Trends in Biochemical Sciences 42(7):516–530. https://doi.org/10.1016/j.tibs.2017.05.001.

[44] Wan, C., Wu, B., Song, Z., Zhang, J., Chu, H., Wang, A., et al., 2015. Insights into the molecular recognition of the granuphilin C2A domain with PI(4,5)P2. Chemistry and Physics of Lipids 186:61–67. https://doi.org/10.1016/j.chemphyslip.2015.01.003.

[45] Philippaert, K., Vennekens, R., 2017. The role of TRP channels in the pancreatic beta-cell. In: 2nd edEmir, T.L.R. (Ed.), Neurobiology of TRP channels. Boca Raton (FL): CRC Press/Taylor & Francis.

[46] Jall, S., Finan, B., Collden, G., Fischer, K., Dong, X., Tschöp, M.H., et al., 2019. Pirt deficiency has subtle female-specific effects on energy and glucose metabolism in mice. Molecular Metabolism. https://doi.org/10.1016/j.molmet.2019.02.011.

[47] Kanno, K., Wu, M.K., Scapa, E.F., Roderick, S.L., Cohen, D.E., 2007. Structure and function of phosphatidylcholine transfer protein (PC-TP)/StarD2. Biochimica et Biophysica Acta (BBA) - Molecular and Cell Biology of Lipids 1771(6):654–662. https://doi.org/10.1016/j.bbalip.2007.04.003.

[48] Hussain, S.S., Harris, M.T., Kreutzberger, A.J.B., Inouye, C.M., Doyle, C.A., Castle, A.M., et al., 2018. Control of insulin granule formation and function by the ABC transporters ABCG1 and ABCA1 and by oxysterol binding protein OSBP. Molecular Biology of the Cell 29(10):1238–1257. https://doi.org/10.1091/mbc.E17-08-0519.

[49] Lyakhova, T.A., Knight, J.D., 2014. The C2 domains of granuphilin are high-affinity sensors for plasma membrane lipids. Chemistry and Physics of Lipids 182:29–37. https://doi.org/10.1016/j.chemphyslip.2013.10.009.

[50] Kanno, K., Wu, M.K., Agate, D.S., Fanelli, B.J., Wagle, N., Scapa, E.F., et al., 2007. Interacting proteins dictate function of the minimal START domain phosphatidylcholine transfer protein/StarD2. Journal of Biological Chemistry 282(42):30728–30736. https://doi.org/10.1074/jbc.M703745200.

[51] Zhou, Q., Zhou, P., Wang, A.L., Wu, D., Zhao, M., Südhof, T.C., et al., 2017. The primed SNARE–complexin–synaptotagmin complex for neuronal exocytosis. Nature 548(7668):420–425. https://doi.org/10.1038/nature23484.

[52] Mitchell, R.K., Hu, M., Chabosseau, P.L., Cane, M.C., Meur, G., Bellomo, E.A., et al., 2016. Molecular genetic regulation of slc30a8/ZnT8 reveals a positive association with glucose tolerance. Molecular Endocrinology 30(1):77–91. https://doi.org/10.1210/me.2015-1227.

[53] Merriman, C., Huang, Q., Rutter, G.A., Fu, D., 2016. Lipid-tuned zinc transport activity of human ZnT8 protein correlates with risk for type-2 diabetes. Journal of Biological Chemistry 291(53):26950–26957. https://doi.org/10.1074/jbc.M116.764605.

[54] Rhodes, C.J., Halban, P.A., 1987. Newly synthesized proinsulin/insulin and stored insulin are released from pancreatic B cells predominantly via a regulated, rather than a constitutive, pathway. The Journal of Cell Biology 105(1):145–153. https://doi.org/10.1083/jcb.105.1.145.

[55] Ivanova, A., Kalaidzidis, Y., Dirkx, R., Sarov, M., Gerlach, M., Schroth-Diez, B., et al., 2013. Age-dependent labeling and imaging of insulin secretory granules. Diabetes 62(11):3687–3696. https://doi.org/10.2337/db12-1819.

[56] Arvan, P., Kuliawat, R., Prabakaran, D., Zavacki, A.M., Elahi, D., Wang, S., et al., 1991. Protein discharge from immature secretory granules displays both regulated and constitutive characteristics. Journal of Biological Chemistry 266(22):14171–14174.

[57] Arvan, P., Halban, P.A., 2004. Sorting ourselves out: seeking consensus on trafficking in the beta-cell. Traffic 5(1):53–61. https://doi.org/10.1111/j.1600-0854.2004.00152.x.

[58] Kuliawat, R., Klumperman, J., Ludwig, T., Arvan, P., 1997. Differential sorting of lysosomal enzymes out of the regulated secretory pathway in pancreatic β-

cells. The Journal of Cell Biology 137(3):595–608. https://doi.org/10.1083/jcb.137.3.595.

[59] Tamaki, M., Fujitani, Y., Hara, A., Uchida, T., Tamura, Y., Takeno, K., et al., 2013. The diabetes-susceptible gene SLC30A8/ZnT8 regulates hepatic insulin clearance. Journal of Clinical Investigation 123(10):4513–4524. https://doi.org/10.1172/JCI68807.

[60] Prost, A.-L., Bloc, A., Hussy, N., Derand, R., Vivaudou, M., n.d. Zinc is both an intracellular and extracellular regulator of KATP channel function. The Journal of Physiology 559(1): 157–167, Doi: 10.1113/jphysiol.2004.065094.

[61] Bancila, V., Cens, T., Monnier, D., Chanson, F., Faure, C., Dunant, Y., et al., 2005. Two SUR1-specific histidine residues mandatory for zinc-induced activation of the rat KATP channel. Journal of Biological Chemistry 280(10): 8793–8799. https://doi.org/10.1074/jbc.M413426200.

[62] Nielsen, T., Sparsø, T., Grarup, N., Jørgensen, T., Pisinger, C., Witte, D.R., et al., 2011. Type 2 diabetes risk allele near CENTD2 is associated with decreased glucose-stimulated insulin release. Diabetologia 54(5):1052–1056. https://doi.org/10.1007/s00125-011-2054-3.

[63] Bogan, J.S., Xu, Y., Hao, M., 2012. Cholesterol accumulation increases insulin granule size and impairs membrane trafficking. Traffic 13(11):1466–1480. https://doi.org/10.1111/j.1600-0854.2012.01407.x.

[64] Sturek, J.M., Castle, J.D., Trace, A.P., Page, L.C., Castle, A.M., Evans-Molina, C., et al., 2010. An intracellular role for ABCG1-mediated cholesterol transport in the regulated secretory pathway of mouse pancreatic β cells. Journal of Clinical Investigation 120(7):2575–2589. https://doi.org/10.1172/JCI41280.

[65] Hao, M., Bogan, J.S., 2009. Cholesterol regulates glucose-stimulated insulin secretion through phosphatidylinositol 4,5-bisphosphate. Journal of Biological Chemistry 284(43):29489–29498. https://doi.org/10.1074/jbc.M109.038034.

[66] Brunham, L.R., Kruit, J.K., Pape, T.D., Timmins, J.M., Reuwer, A.Q., Vasanji, Z., et al., 2007. Beta-cell ABCA1 influences insulin secretion, glucose homeostasis and response to thiazolidinedione treatment. Nature Medicine 13(3):340–347. https://doi.org/10.1038/nm1546.

[67] Guo, W., Gong, Y., Fu, Z., Fu, J., Sun, Y., Ju, X., et al., 2016. The effect of cholesteryl ester transfer protein on pancreatic beta cell dysfunction in mice. Nutrition and Metabolism 13:21. https://doi.org/10.1186/s12986-016-0082-1.

[68] Xia, F., Xie, L., Mihic, A., Gao, X., Chen, Y., Gaisano, H.Y., et al., 2008. Inhibition of cholesterol biosynthesis impairs insulin secretion and voltage-gated calcium channel function in pancreatic beta-cells. Endocrinology 149(10): 5136–5145. https://doi.org/10.1210/en.2008-0161.

[69] Hao, M., Head, W.S., Gunawardana, S.C., Hasty, A.H., Piston, D.W., 2007. Direct effect of cholesterol on insulin secretion: a novel mechanism for pancreatic beta-cell dysfunction. Diabetes 56(9):2328–2338. https://doi.org/10.2337/db07-0056.

[70] MacDonald, M.J., Ade, L., Ntambi, J.M., Ansari, I.-U.H., Stoker, S.W., 2015. Characterization of phospholipids in insulin secretory granules and mitochondria in pancreatic beta cells and their changes with glucose stimulation. Journal of Biological Chemistry 290(17):11075–11092. https://doi.org/10.1074/jbc.M114.628420.

[71] Ohashi, M., de Vries, K.J., Frank, R., Snoek, G., Bankaitis, V., Wirtz, K., et al., 1995. A role for phosphatidylinositol transfer protein in secretory vesicle formation. Nature 377(6549):544–547. https://doi.org/10.1038/377544a0.

[72] Nguyen, P.M., Gandasi, N.R., Xie, B., Sugahara, S., Xu, Y., Idevall-Hagren, O., 2019. The PI(4)P phosphatase Sac2 controls insulin granule docking and release. The Journal of Cell Biology. https://doi.org/10.1083/jcb.201903121.

[73] Wen, P.J., Osborne, S.L., Morrow, I.C., Parton, R.G., Domin, J., Meunier, F.A., 2008. Ca2+-regulated pool of phosphatidylinositol-3-phosphate produced by phosphatidylinositol 3-kinase C2alpha on neurosecretory vesicles. Molecular Biology of the Cell 19(12):5593–5603. https://doi.org/10.1091/mbc.e08-06-0595.

[74] Dominguez, V., Raimondi, C., Somanath, S., Bugliani, M., Loder, M.K., Edling, C.E., et al., 2011. Class II phosphoinositide 3-kinase regulates exocytosis of insulin granules in pancreatic beta cells. Journal of Biological Chemistry 286(6):4216–4225. https://doi.org/10.1074/jbc.M110.200295.

[75] Gromada, J., Bark, C., Smidt, K., Efanov, A.M., Janson, J., Mandic, S.A., et al., 2005. Neuronal calcium sensor-1 potentiates glucose-dependent exocytosis in pancreatic β cells through activation of phosphatidylinositol 4-kinase β. Proceedings of the National Academy of Sciences 102(29):10303–10308 https://doi.org/10.1073/pnas.0504487102.

[76] Xie, B., Nguyen, P.M., Guček, A., Thonig, A., Barg, S., Idevall-Hagren, O., 2016. Plasma membrane phosphatidylinositol 4,5-bisphosphate regulates Ca(2+)-influx and insulin secretion from pancreatic β cells. Cell Chemical Biology 23(7):816–826. https://doi.org/10.1016/j.chembiol.2016.06.009.

[77] Shyng, S.-L., Nichols, C.G., 1998. Membrane phospholipid control of nucleotide sensitivity of K$_{ATP}$ channels. Science 282(5391):1138–1141.

[78] Jiang, Z., Redfern, R.E., Isler, Y., Ross, A.H., Gericke, A., 2014. Cholesterol stabilizes fluid phosphoinositide domains. Chemistry and Physics of Lipids 182:52–61. https://doi.org/10.1016/j.chemphyslip.2014.02.003.

[79] Wang, H., Ma, Q., Qi, Y., Dong, J., Du, X., Rae, J., et al., 2019. ORP2 delivers cholesterol to the plasma membrane in exchange for phosphatidylinositol 4, 5-bisphosphate (PI(4,5)P2). Molecular Cell 73(3):458–473. https://doi.org/10.1016/j.molcel.2018.11.014 e7.

[80] Lees, J.A., Messa, M., Sun, E.W., Wheeler, H., Torta, F., Wenk, M.R., et al., 2017. Lipid transport by TMEM24 at ER-plasma membrane contacts regulates pulsatile insulin secretion. Science 355(6326). https://doi.org/10.1126/science.aah6171.

